

AD \_\_\_\_\_

Award Number: DAMD17-97-1-7079

TITLE: NMR Reconstructive Elasticity Imaging of Breast:  
Surrogate Remote Palpation Using Quantitative 3-D  
Displacement and Strain Estimations

PRINCIPAL INVESTIGATOR: Thomas L. Chenevert, Ph.D.

CONTRACTING ORGANIZATION: University of Michigan  
Ann Arbor, Michigan 48109-1274

REPORT DATE: September 1999

TYPE OF REPORT: Annual

PREPARED FOR: U.S. Army Medical Research and Materiel Command  
Fort Detrick, Maryland 21702-5012

DISTRIBUTION STATEMENT: Approved for Public Release;  
Distribution Unlimited

The views, opinions and/or findings contained in this report are those of the author(s) and should not be construed as an official Department of the Army position, policy or decision unless so designated by other documentation.

DEC CLASSIFIED 4  
20010124 090

REPORT DOCUMENTATION PAGE			Form Approved OMB No. 074-0188	
Public reporting burden for this collection of information is estimated to average 1 hour per response, including the time for reviewing instructions, searching existing data sources, gathering and maintaining the data needed, and completing and reviewing this collection of information. Send comments regarding this burden estimate or any other aspect of this collection of information, including suggestions for reducing this burden to Washington Headquarters Services, Directorate for Information Operations and Reports, 1215 Jefferson Davis Highway, Suite 1204, Arlington, VA 22202-4302, and to the Office of Management and Budget, Paperwork Reduction Project (0704-0188), Washington, DC 20503				
1. AGENCY USE ONLY (Leave blank)	2. REPORT DATE September 1999	3. REPORT TYPE AND DATES COVERED Annual (11 Aug 98 - 10 Aug 99)		
4. TITLE AND SUBTITLE NMR Reconstructive Elasticity Imaging of Breast: Surrogate Remote Palpation Using Quantitative 3-D Displacement and Strain Estimations		5. FUNDING NUMBERS DAMD17-97-1-7079		
6. AUTHOR(S) Thomas L. Chenevert, Ph.D.				
7. PERFORMING ORGANIZATION NAME(S) AND ADDRESS(ES)  University of Michigan Ann Arbor, Michigan 48109-1274 E-MAIL: tchenev@umich.edu		8. PERFORMING ORGANIZATION REPORT NUMBER		
9. SPONSORING / MONITORING AGENCY NAME(S) AND ADDRESS(ES)  U.S. Army Medical Research and Materiel Command Fort Detrick, Maryland 21702-5012		10. SPONSORING / MONITORING AGENCY REPORT NUMBER		
11. SUPPLEMENTARY NOTES				
12a. DISTRIBUTION / AVAILABILITY STATEMENT Approved for public release; distribution unlimited			12b. DISTRIBUTION CODE	
13. ABSTRACT (Maximum 200 Words)  The goal of this research program is to develop a sensitive diagnostic technique based on quantitative elasticity imaging permitting surrogate palpation of deep lying breast lesions. The remote measurement of elasticity in breast tissues may provide unique information which could increase detection and/or characterization of potentially malignant masses not accessible to manual palpation. The primary technical objective of this study is to refine and test an MRI method for the acquisition of high resolution 3-dimensional (3D) spatial displacement data through the imaged object for quantitative estimation of internal strain and elastic modulus. Proof-of-concept of the proposed 3D displacement-encoding, stimulated echo technique has been completed and published using two-dimensional test objects. A pneumatically-driven deformation device under acquisition sequence control has been designed, constructed, and demonstrated to produce highly reproducible deformations of the imaged object. The image acquisition sequence has been generalized to encode 3D displacements over a 3D volume using "classic" 3D and fast-spin-echo schemes. Volumetric datasets of 3D phantoms have been acquired and submitted for processing using newly developed 3D elasticity reconstruction algorithms. Comparisons between 2D and 3D elasticity reconstructions from simulated and experimental displacement data shows higher accuracy of the 3D elasticity reconstruction.				
14. SUBJECT TERMS  Breast Cancer; Tissue Elasticity; Magnetic Resonance Imaging; Models			15. NUMBER OF PAGES 47	
			16. PRICE CODE	
17. SECURITY CLASSIFICATION OF REPORT Unclassified	18. SECURITY CLASSIFICATION OF THIS PAGE Unclassified	19. SECURITY CLASSIFICATION OF ABSTRACT Unclassified	20. LIMITATION OF ABSTRACT Unlimited	

## FOREWORD

Opinions, interpretations, conclusions and recommendations are those of the author and are not necessarily endorsed by the U.S. Army.

NA Where copyrighted material is quoted, permission has been obtained to use such material.

NA Where material from documents designated for limited distribution is quoted, permission has been obtained to use the material.

PK Citations of commercial organizations and trade names in this report do not constitute an official Department of Army endorsement or approval of the products or services of these organizations.

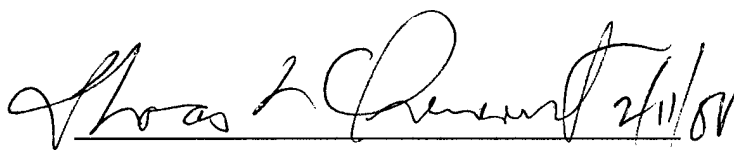
X In conducting research using animals, the investigator(s) adhered to the "Guide for the Care and Use of Laboratory Animals," prepared by the Committee on Care and use of Laboratory Animals of the Institute of Laboratory Resources, national Research Council (NIH Publication No. 86-23, Revised 1985).

X For the protection of human subjects, the investigator(s) adhered to policies of applicable Federal Law 45 CFR 46.

N/A In conducting research utilizing recombinant DNA technology, the investigator(s) adhered to current guidelines promulgated by the National Institutes of Health.

N/A In the conduct of research utilizing recombinant DNA, the investigator(s) adhered to the NIH Guidelines for Research Involving Recombinant DNA Molecules.

N/A In the conduct of research involving hazardous organisms, the investigator(s) adhered to the CDC-NIH Guide for Biosafety in Microbiological and Biomedical Laboratories.

  
PI - Signature                      Date

<b><u>TABLE OF CONTENTS</u></b>	<b><u>Page</u></b>
<b>INTRODUCTION</b>	<b>2</b>
<b>METHODS AND RESULTS PER TASK</b>	<b>2 - 12</b>
<b>CONCLUSIONS</b>	<b>12</b>
<b>REFERENCES</b>	<b>13</b>

#### **APPENDIX**

Reprint of: "Elasticity reconstructive imaging via stimulated echo MRI," T.L. Chenevert, A.R. Skovoroda, M. O'Donnell, and S.Y. Emelianov, Magnetic Resonance in Medicine, 39, pp. 482-490 (1998).

Manuscript of: "Three-dimensional static displacement, stimulated echo NMR elasticity imaging,"

Derek D. Steele, Thomas L. Chenevert, Andrei R. Skovoroda and Stanislav Y. Emelianov, submitted to Physics in Medicine and Biology.

Chenevert, TL, Steele, DD, Emelianov, SY and Shovoroda, AR. Three-Dimensional Static Displacement Stimulated-Echo NMR Strain Imaging. Proceedings of the International Society of Magnetic Resonance in Medicine 1999; 263.

Steel, DD and Chenevert, TL, Emelianov, SY, and O'Donnell, M. Signal-to-Noise Consideration in Static Displacement, Stimulated Echo NMR Elasticity Imaging. Proceedings of the International Society of Magnetic Resonance in Medicine 1999; 1616.

## INTRODUCTION

While manual palpation remains the first diagnostic line of defense against breast cancer[1-4], it is unfortunately limited to relatively large and superficial lesions. The central hypothesis of this work is that remote measurement of elasticity in breast tissues is possible and provides unique information which could increase detection and/or characterization of potentially malignant masses not manually accessible. Our preliminary studies suggest that the proposed methods are capable of precisely measuring internal deformation and strain in three dimensions. These data are required to reconstruct the elasticity distribution within the object. Consequently, technologies developed within the scope of this project may have significant diagnostic value in detection and management of breast cancer.

Most elastography to date has utilized ultrasound [5-14], although MRI has also been used [15-22]. Usually an external static or dynamic deformation is applied while the resultant displacement or propagating shear wave is documented by imaging devices. In general, to reconstruct the tissue-specific property of Young's modulus in complex systems such as the breast, the 3-D displacement vector must be measured over a 3-D volume. In this project, we are developing techniques that measure the 3-D displacement vector over any volume in the object at high spatial resolution. These data will be processed to produce 3-D strain images for submission to a 3D elasticity reconstruction routine to map the relative Young's modulus within the volume.

## ACCOMPLISHMENTS IN RELATION TO STATEMENT OF WORK

The goal of this research program is to develop a sensitive diagnostic technique based on quantitative elasticity imaging permitting surrogate palpation of deep lying breast lesions. To this end, specific technical objectives/tasks were adopted and summarized in the proposal Statement of Work. Each task is restated below along with descriptions of relevant Methods and Progress/Results.

### Technical Objective I: Data Acquisition and Reconstruction

#### Task 1: Month 1-3

*Construction of computer controlled hydraulic compression device capable of producing an incremental surface deformation of the mechanical body. This device will be triggered by NMR imaging system and have a simple timing/displacement control appropriate for phantom studies.*

The proposed method requires that the imaged object experience a relatively minor externally-applied deformation force. Based on signal optimization simulations, differential deformations below 10% (e.g., <1cm deformation across a 10cm object) should be adequate for generation of elasticity maps. Design details of the mechanical deformation device were provided in Year 1 Progress Report, although are briefly summarized here with the device schematic is shown in Figure 1. Four neoprene bellows outside of the NMR coil (rf-coil) provide both upward and downward force to an acrylic plate on top of the phantom. The top bellows are on a common pressure circuit, likewise the bottom pair are pressurized together to yield uniform vertical displacement along the

top of phantom. Solid acrylic yolks at both ends of the device insure that only the top plate moves in response to pressurization. Pneumatic elements are driven by air-pressure solenoid valves that are, in turn, controlled by a transistor-transistor-logic circuit triggered by the NMR imaging sequence.

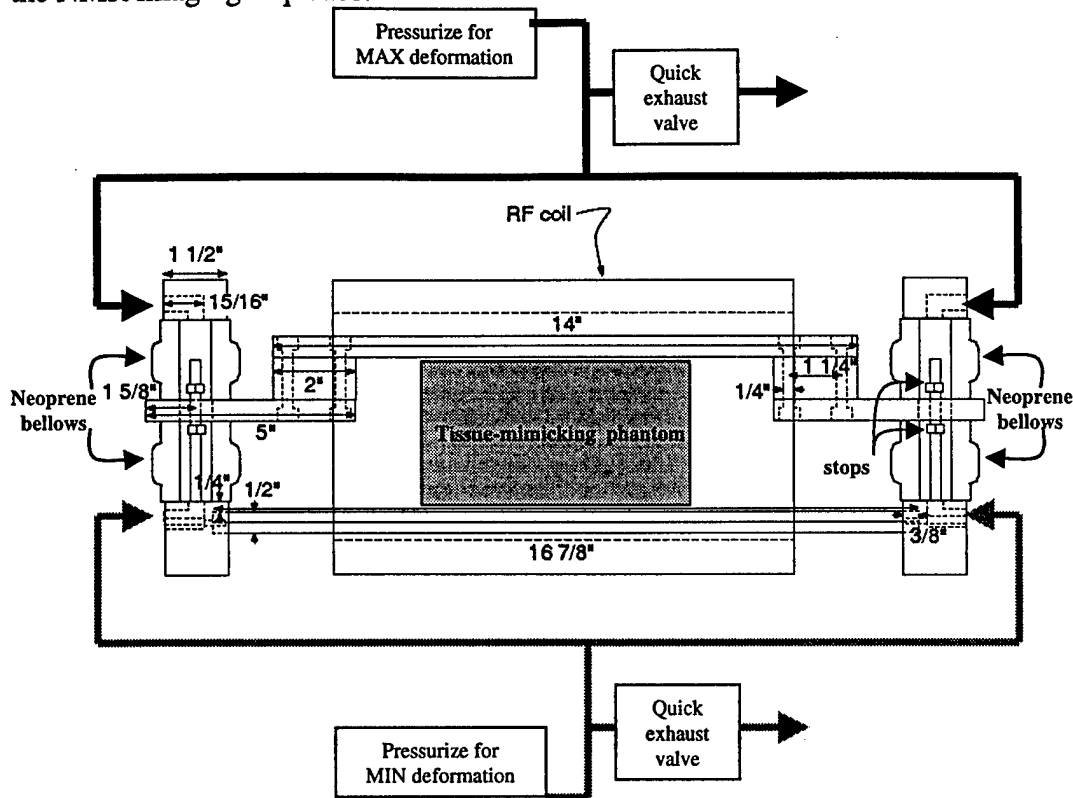


Figure 1. Side-view schematic of pneumatic deformation system.

Phase-encode MRI methods, as employed here, require that data are acquired in many segments over an extended period of time. Consequently the mechanical deformation must be highly reproducible for each segment. Mechanical stability tests of the device were performed using a slightly modified version of the 2D-displacement encoding MRI sequence. The upshot of these tests was that the system is extremely stable and reproducible in application of a 5mm differential deformation (mixing time,  $T_M=350\text{msec}$ ). The observed phase instabilities were barely above that allowed by NMR signal limits. These results suggest mechanical reproducibility within  $<20\text{microns}$ . One significant finding of these stability tests was that the mechanical response of the deformation device was significantly faster ( $\sim 150\text{ms}$ ) than the "settling time" of the tissue-mimicking phantoms ( $\sim 350\text{ms}$ ). That is, internal mechanical reflected waves persist beyond point the acrylic drive plates stop. We anticipate that breast tissue will have comparably long settling times, thus we will continue to use long mixing times ( $\sim 350\text{ms}$ ) in our experiments despite the SNR gains of shorter times. Immunity to long persistence mechanical waves was *the* main motivation to use the stimulated-echo approach as is done here.

Task 2: Month 1-6

*Development of various phantoms to test NMR displacement and strain data acquisition and 3-D elasticity reconstruction algorithms.*

Fabrication of phantoms to model the mechanical and NMR properties of human tissue is an important step in development and verification of optimized NMR displacement-encoded volume simulated-echo pulse sequence. Moreover, simple geometries of phantoms allow characterization of the elasticity reconstruction algorithms. The phantom materials should closely resemble relevant tissue properties. In addition, these materials should be stable (i.e. months) and permit the non-destructive embedding of lesion-equivalent targets within the phantom.

We have previously developed tissue-mimicking phantoms to test NMR elasticity imaging device. These phantoms were made of two materials: a) polymer produced by M-F Manufacturing Co., Inc. (Fort Worth, TX), and b) gelatin (Sigma-Aldrich Co., 3050 Spruce Street, St. Louis, MO 63103 USA). The first material, plastisol, consists of a liquid plastic combined with either softener (plasticizer) or hardener. By varying the proportion of these two components, it is possible to produce composite models of desired elasticity. The raw composite materials were stirred and heated to approximately 170°C. At that temperature the mixture was poured into molds producing a tissue-mimicking time-stable phantom of desired shape and elasticity distribution. However, two major deficiencies remain. First, plastisol does not have desired tissue equivalent NMR properties. Second, due to high temperature rise during phantom preparation, it is impossible to produce tissue-containing phantoms using plastisol.

Several different materials were further considered for NMR elasticity phantoms. These materials include Semicosil 921, Semicosil 905 and Silgel 612 (Wacker Silicones Co., Adrian, MI 49221), and Rhodorsil RTV 163 (Rhone-Poulenc, France). From all tested materials, the Semocosil 921 silicone gel appeared to mimic the tissue properties the best. The elasticity of silicone gel can be simply controlled by mixing ratio of two components. The composite material is then poured into the mold and cured at the room temperature enabling fabrication of tissue containing phantoms. These silicone gels have shown high SNR spin-echo signal over the range of hardness variations. In addition, the mechanical properties of silicone did not change over 60 days, as was measured by Instron-type mechanical system. Therefore, it is possible to fabricate tissue-mimicking phantoms of desired shape and elasticity distribution using Semicosil 921 silicone gel.

Based on favorable NMR and mechanical properties, phantoms were fabricated using the Semicosil materials. These phantoms were designed with simple geometries to assess spatial resolution and accuracy of 3D strain imaging 3D elasticity reconstruction algorithms, and include crossed bars of hard material (6x Young's modulus) with variable size and separation (for resolution) and simple spherical inclusions for comparison with theoretical results.

**Task 3: Month 1-12**

*Development of the NMR displacement-encoded, volume stimulated-echo pulse sequence optimized for displacement/strain sensitivity and SNR.*

Two, 3D displacement-encode, volume stimulated-echo pulse sequences have been developed. These are shown in Figure 2(a) using "classic" 3D spatial encoding, and (b) a fast-spin-echo (FSE) extension to more efficiently encode the 3<sup>rd</sup> dimension. The classic 3D sequence, is simplest and implement but unfortunately it is clinically

impractical due to very long scantimes. For example, acquisition of volumetric data at 256x128 matrix resolution over 16 slices with full 3-axis displacement sensitivity typically requires 1-2hours (if  $TR=1\text{sec}$ ;  $TR \times 128 \times 16 \times 3 = 1.7\text{hrs}$ ). Incorporation of the FSE echo train permits a scantime reduction by a factor of 1/4, 1/8, to 1/16 dependent on echo train length. To date, we have implemented an 8-echo FSE sequence where the FSE phase-encoding is applied along the 3<sup>rd</sup> dimension (i.e. slice direction). Ideally, all slice encode steps are acquired in one-shot which greatly reduces scan time (to 13min). Unfortunately, it appears that poor gradient hardware performance is introducing eddy current effects that confound 3<sup>rd</sup> axis encoding on our 2T MRI system. Phase shifts from this artifact derail strain measurement based on phase. We are in the process of evaluating means to apply phase corrections to reduce imperfections in the FSE component of the sequence.

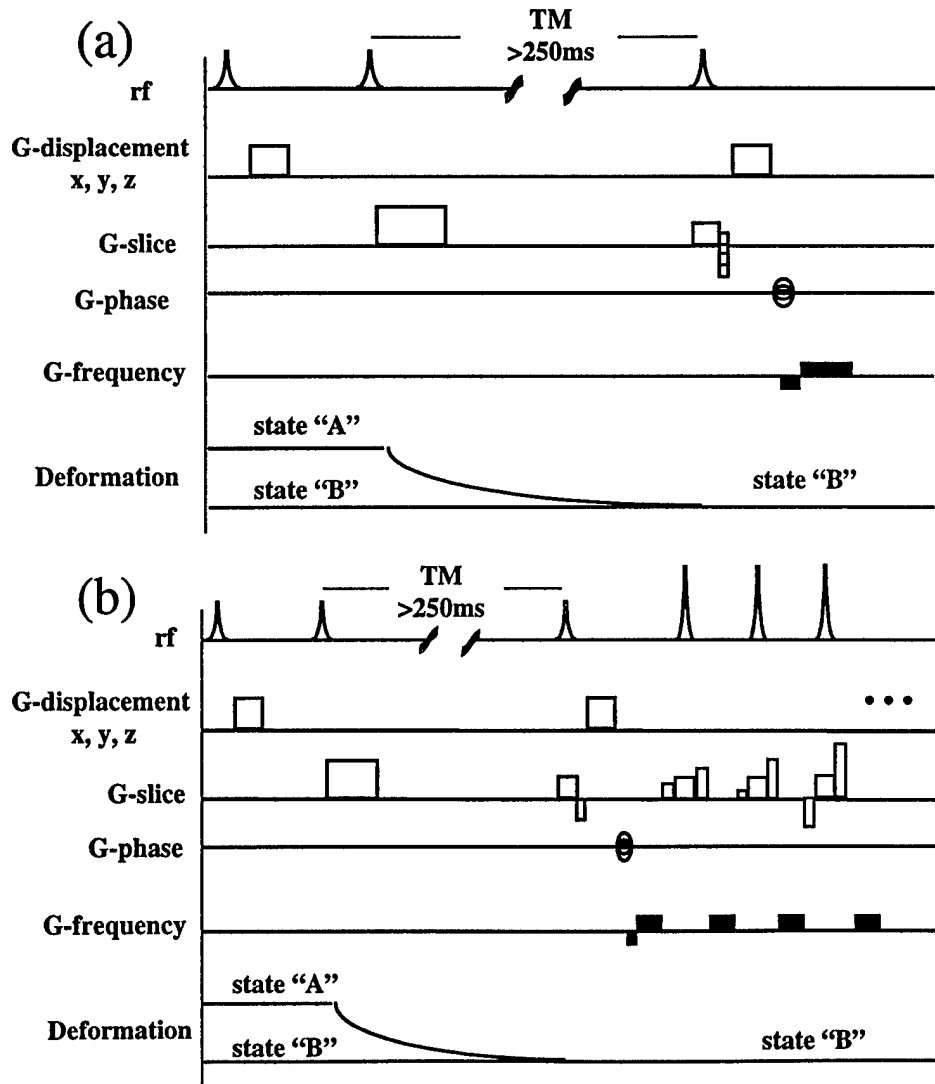


Figure 2. Volumetric displacement-encoding stimulated echo sequences using (a) classic 3D encoding and (b) fast-spin-echo encoding of the third dimension.



Images of tissue mimicking phantom containing ramped bars of harder material acquired via the 3D FSE stimulated echo sequence are shown in Figure 3. Spurious intensity modulations in the magnitude image (i.e. conventional MRI contrast) in Figure 3(a) indicate an imperfect reconstruction along the 3<sup>rd</sup> dimension. That is, there is an interference of signal from adjacent slices. Despite this, derivative displacement and strain images display features of the object (Figure 3(b-f)), however, residual phase error prevent acceptable elasticity reconstructions. Deformation and object symmetry meant the displacement and strain in the 3<sup>rd</sup> dimension (ie. perpendicular to the image) was small. This material was presented at the 1999 International Society of Magnetic Resonance Medicine (ISMRM) and is included in the appendix.

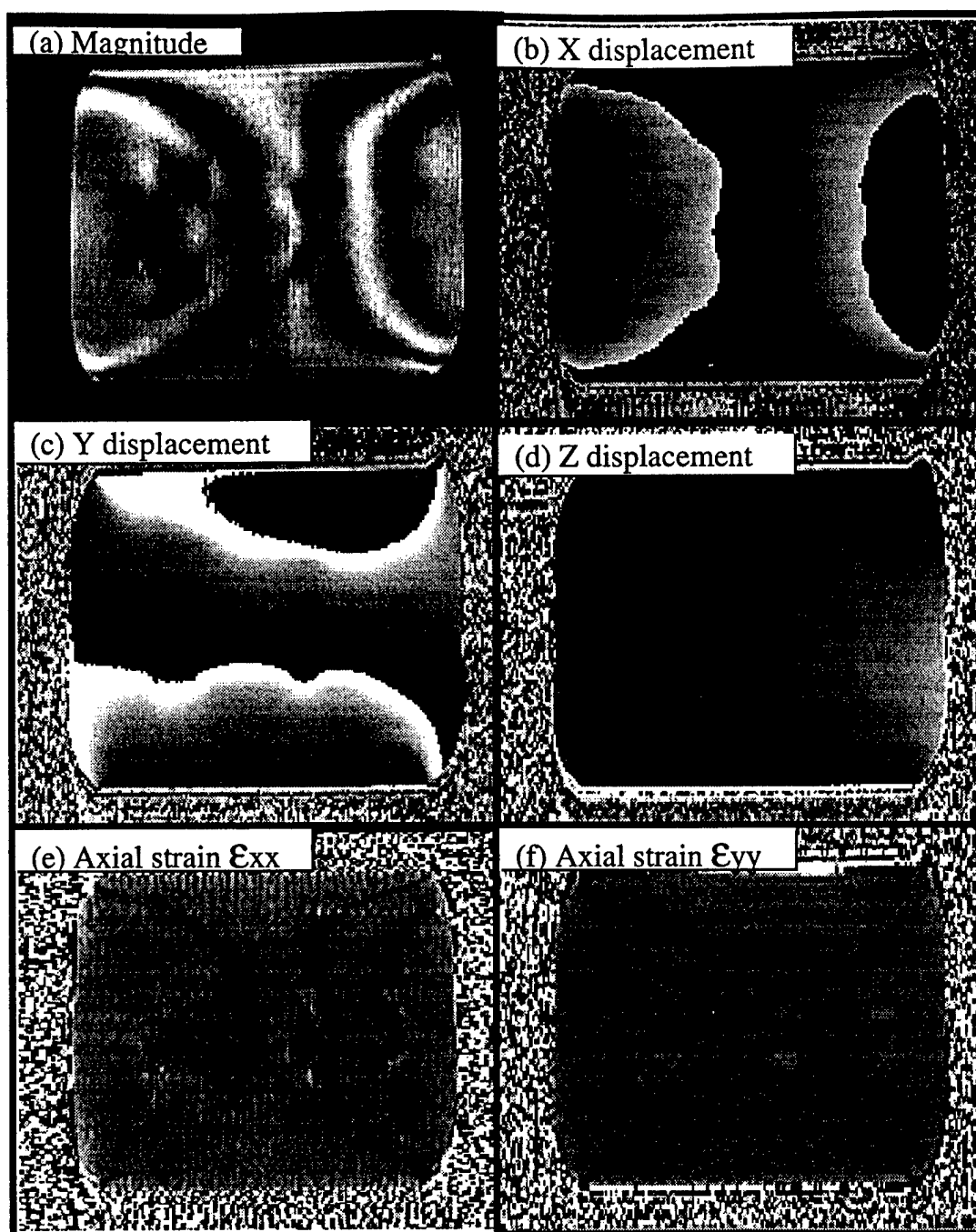


Figure 3. Volumetric displacement-encoding stimulated echo sequence applied to Semicosil rubber phantom containing crossed ramped bars of hard material. Shown are (a) magnitude image, displacement images in (b) X right-to-left, (c) Y top-to-bottom, and (d) Z through-plane. Strain images (i.e. spatial derivative of displacement) for X and Y displacements are shown in (e) and (f) respectively.

Computer simulations were performed to address the tradeoff between displacement sensitivity and NMR signal-to-noise (SNR) since optimization of one parameter comes at the expense of another. Key parameters that affect SNR and displacement sensitivity include: displacement gradient amplitude and duration; applied deformation amplitude; image resolution; mixing time,  $T_M$ ; and tissue water diffusion properties. Results of the

optimization studies suggest greater SNR can be achieved through greater surface strain (i.e. deformation of the object by  $\sim 10\%$ ) with a corresponding reduction in displacement encoding (reduced from 4 to 1 gauss/cm). Increasing the applied deformation will have the added benefit to make the applied deformation more significant relative to "background" physiologic motions such as cardiac and respiratory. Yet higher deformation, however, introduce the need to consider non-linear elastic effects (see Task 5). These optimization studies were also presented at the 1999 International Society of Magnetic Resonance Medicine. The abstract is included in the Appendix.

#### Task 4: Month 1-12

*Expansion of previously developed linear elasticity reconstruction algorithms for volumetric displacement and strain NMR measurements.*

Expansion of linear elasticity reconstruction algorithms were focused on the following two aspects: a) development of boundary detection methods to identify the regions of uniform elasticity (Young's modulus) distribution, and b) development of volumetric linear elasticity reconstruction algorithms for optimized NMR displacement-encoded, volume simulated-echo pulse sequence.

The boundary detection algorithm was developed for specifically NMR elasticity imaging. This algorithm is based on the stress continuity condition applicable for soft tissue deformations used in these studies. The relevant boundary definition methods were detailed in the Year 1 Progress Report.

The following relates to extensions to a 3D elasticity reconstruction algorithm wherein complete three-dimensional strain data are required to solve for a general, three-dimensional object. Previously, only 2D reconstruction algorithms have been applied, yet these are anticipated to lead to errors at planes where through-plane strain is significant. As an illustration, Figure 4 shows simulated elasticity distributions at a slice just within ( $z=0.95$  radius) and just outside ( $z=1.05$  radius) of a hard spherical inclusion. These data were used to test the 3D elasticity reconstruction algorithm and provide supportive evidence for the need of 3D reconstruction algorithms in general.

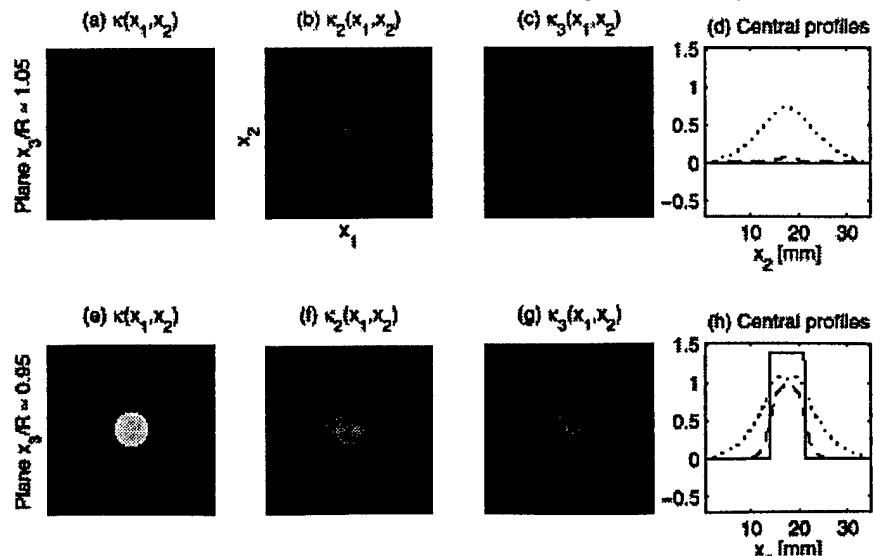


Figure 4. Simulated elasticity maps at planes just outside of (top row) and just within of (bottom row) a spherical hard inclusion. The 3D reconstruction,  $\kappa_3$ , (images on right) was a more faithful depiction of truth,  $\kappa$ , (images on left), relative to the 2D reconstruction,  $\kappa_2$ , (images in middle).

**Task 5: Month 10-26**

*Development of the nonlinear elasticity reconstruction model capable to process high-strain NMR images.*

The elasticity reconstruction problem can be posed in number of ways depending on the experimental conditions such as amount of surface deformations, type of phantom materials, etc. Previously, we have developed a reconstruction algorithm based on linear theory of elasticity, i.e., applicable for small deformations and linear elastic materials. However, both mechanical equilibrium equations and the displacement-strain relations must include high order spatial derivatives of the displacement if the average deformation is too large to be described with a linear model. An algorithm was developed to reconstruct the elastic modulus of soft tissue for comparatively large surface deformations required for optimal SNR and sensitivity strain/displacement images. Numerical methods were developed to reduce error propagation in reconstruction algorithms.

As said, linear elastic theory is reasonable in the realm of a few percent surface deformation as was used in our initial experiments. Based on optimization studies performed for Task 3, however, greater sensitivity and SNR is available at higher deformation, such as >10%. Consequently, in current experiments we employ surface deformations ~10%. As predicted, at these settings there is sufficient phase contrast of internal deformations with reduced signal losses to diffusion since displacement-encoding gradients are proportionally reduced. Unfortunately, image artifact due to imperfect hardware performance on our 2T unit using the 3D fast-spin-echo (FSE) exceed non-linear effects. Moreover, since the artifact is unrelated to linearity of elastic deformation, application of non-linear algorithm elements is not a remedy to their removal. We have decided to forego application of the non-linear modification of the reconstruction algorithm until we resolve the artifacts in the 3D FSE technique.

**Technical Objective II: Phantom Studies on 2T 18cm Bore MRI System****Task 6: Month 7-22**

*Development of gel- and rubber-based phantoms with tissue mimicking elastic properties. Time stable phantoms with non-palpable inclusions of various shapes and elasticity contrast positioned at different locations within the phantom will be produced.*

During the first year of the project, we have identified and tested the materials for tissue mimicking phantoms. Our ultimate goal is to simulate the anatomical and geometrical features of the normal and pathologically transformed breast using these materials. The models of breast containing single or multiple inclusions were fabricated using plastisol material (M-F Manufacturing Co., Fort Worth, Texas, USA).

Our recent studies, however, suggested that silicone gels could better simulate the mechanical and NMR relaxation properties of the tissue. Initially, silicone-gel based homogeneous phantoms were produced for mechanical and NMR testing (Semicosil 921, Wacker Silicones Co., Adrian, Michigan, USA). These tests showed the material had suitable NMR properties - like tissue. To control mechanical properties, the Semicosil 921 contains two components, A and B, wherein different ratios of these components are used to vary the mechanical properties of the gel. A tissue-mimicking phantom was

constructed in several steps. First, background material was prepared by thoroughly mixing components A and B in a 1:1 ratio, and then pouring the mixture into a 154-mm by 80-mm rectangular mold. The mixture was degassed and cured for 24 hours at room temperature to produce a 22-mm thick layer. Then a 25-mm diameter hard sphere was prepared from a 1:2.5 mixture of A and B and was placed on top of the layer in the middle of the mold. Finally, another batch of background material (1:1 ratio) was poured into the mold resulting in a 64-mm by 80-mm by 154-mm phantom with a single, hard, spherical inclusion roughly in the center. At the same time, three samples of each batch were taken to independently assess the elasticity contrast between the inclusion and surrounding materials. These measurements were performed using the force-deformation system described in (Erkamp et al 1998), and showed that the inclusion was four times harder than the background, and that both background materials were elastically equivalent. These are highly stable and are still in use several months post-fabrication.

#### Task 7: Month 12-26

*Investigation of the capabilities of 3-D NMR elasticity imaging, i.e., determine sensitivity, accuracy and resolution of NMR displacement and strain images, and reconstructed elasticity (Young's modulus) distribution.*

As shown by simulation presented in Figure 4, elasticity maps reconstructed from 3-D strain data should be more accurate than a 2-D elasticity reconstructions. This should be particularly true near the edges of an object where the plane-strain-state is violated; that is where the strain along the "through-plane" direction is non-negligible. This concept was tested on silicone-gel based phantoms developed in Task 6 using the volume stimulated-echo pulse sequence (Task 3). A comparison of the actual "2D" reconstruction and "3D" reconstructed elasticity maps for 2 of 32

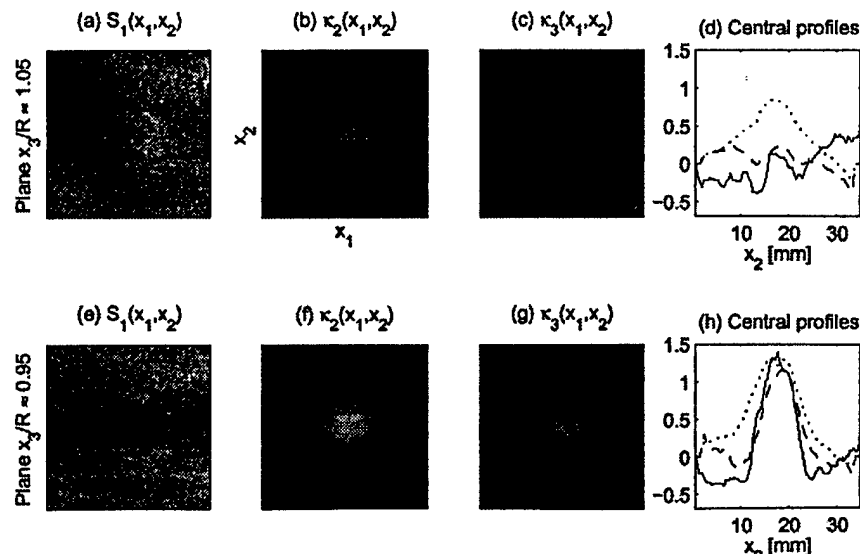


Figure 5. Reconstructed elasticity maps at planes just outside of (top row) and just within (bottom row) a spherical hard inclusion in a silicone-gel phantom. These results are consistent with the simulations (Figure 4) that show the 3D reconstruction,  $\kappa_3$ , (images on right) more faithfully depicts the size of the inclusion.

planes through the phantom data are shown in Figure 5. The planes selected through the phantom and general format of Figure 5 were chosen for direct comparison between the simulation (Figure 4) and experiment (Figure 5). Ideally, there would be no inclusion visible in the plane outside of the inclusion (ie. reconstructions in the top row of Figure 5 should be uniform). Violation of the non-negligible strain remote from the object, however, results in inaccuracies in 2D reconstructions. These errors are clearly reduced in the 3D reconstruction which confirms simulation results.

### **Technical Objective III: Translation to 1.5T Human MRI System**

#### **Task 8: Month 20-25**

*Design and construction of the compression device compatible with human breast NMR imaging system and capable to produce wide range of surface deformations. Development of sophisticated circuits to control surface deformations and time synchronization with human MRI system.*

Translation to the 1.5T unit system has begun. We have a compressor pneumatic-drive system in hand that is suitable for operation on our research 1.5T human MRI unit. Existing phantoms will be used for testing on the 1.5T unit.

#### **Task 9: Month 24-34**

*Development of appropriate for clinical studies 3-D displacement encoded, volume stimulated-echo pulse sequence on human MRI system with data acquisition time within or comparable to regular MRI examination.*

Two- and three-dimensional fast-spin-echo (FSE) are being modified for displacement-sensitive, stimulated-echo acquisitions. We expect to initial sequence testing within a month. When a 32-echo-train-length sequence is realized, without significant system-related artifact, acceptable scan times should be achieved.

#### **Task 10: Month 22-34**

*Development of time efficient elasticity reconstruction algorithms more suitable for clinical applications.*

Our current 3D elasticity reconstruction is extremely long (many hours). Since the reconstruction is a numerical solution to invert high-order differential equations, reconstruction time scales with the acquired quantity of slices and the in-plane resolution. Previously, volumetric datasets, as generated in this project did not exist, thus not all practical issues related to 3D elasticity reconstruction were known. To date, most programming efforts have been directed to management of the acquired six-dimensional datasets (i.e. position in x,y,z, and displacement-sensitive  $u_x, u_y, u_z$ ) which expand to and a "12-vector" per pixel (position, and 9-elements of the strain tensor). The 12-dimensional data is only the *input* to the reconstruction. Unfortunately, given these management issues, to date there has not been significant

progress toward improving reconstruction efficiency. Greater interest is being paid to validation of the reconstructions rather than reconstruction speed.

**Task 11: Month 20-30**

*Estimate the influence of the cardiac and respiratory motion to elasticity images and develop the approaches to reduce these artifacts.*

Resolution of systematic artifacts that originate from imperfect hardware performance are more pressing than estimation of patient-originated artifact. As such, action on Task 11 are postponed until we have an operational sequence on the 1.5T unit. We anticipate significantly greater performance on the 1.5T unit which routinely provides 32-echo-train-length images without apparent artifact.

**Task 12: Month 30-36**

*Validation of clinical NMR data acquisition and elasticity reconstruction methods on breast tissue mimicking phantoms.*

**CONCLUSIONS**

Tasks to design, fabricate and refine the "deformation device", essential for phantom studies, is complete. The MRI-compatible hardware, pneumatic components, and control circuitry are now fully operational. This device provides excellent control and stability in repetitive deformations of an tissue-mimicking objects. Significant effort was directed to develop suitable phantom materials. Requirements include: temporally stable (over months-years); adjustable mechanical properties to match a range of tissues; moldable to simple geometries; tissue-like NMR properties. The Semocsil 921 silicone gel generally meets these requirements (with the exception of tissue-like diffusion) and will be used in subsequent phantom studies. Three-dimensional, stimulated-echo acquisition sequences that have sensitivity to 3-dimensional displacement have been written and applied to gather 3D strain data on simple objects. These data have been input in newly-designed 3D elasticity reconstruction routines to yield, to the best of our knowledge, the first elasticity reconstruction based on volumetric internal spatial/strain data. Methods to reduce data acquisition time, via stimulated-echo spatial encoding have not yet been satisfactory in terms of artifact control. We believe these artifacts are due to the particular MRI unit used, and have thus begun to move experiments to the 1.5 T human MRI unit which is known to have better performance.

## References

1. A. P. Sarvazyan, A. R. Skovoroda, S. Y. Emelianov, J. B. Fowlkes, J. G. Pipe, R. S. Adler, R. B. Buxton, P. L. Carson, "Biophysical Bases of Elasticity Imaging. Acoustical Imaging," 21, Plenum Press, New York, p. 223-240, 1995.
2. A. R. Skovoroda, A. N. Klishko, D. A. Gukasyan, E. I. Maevsky, V. D. Ermilova, G. A. Oranskaya, and A. P. Sarvazyan, Quantitative analysis of the mechanical characteristics of pathologically altered soft biological tissues. *Biofizika*, 40(6), 1335-1340, (1995).
3. D. Hill, V. White, D. Jolley, Mapperson, Self examination of the breast: is it beneficial? Meta-analysis of studies investigating breast self examination and the extent of disease in patients with breast cancer. *Br J Med* 297, 271-275 (1988).
4. P. A. Newcomb, S. Weiss, B. E. Storer, D. Scholes, B. E. Young, Breast self examination in relation to the occurrence of advanced breast cancer. *J Natl Cancer Inst* 83, 260-265 (1991).
5. R. J. Dickinson, C. R. Hill, Measurement of soft tissue motion using correlation between A-scans. *Ultrasound Med Biol* 8, 263-271 (1982).
6. M. Tristam, D. C. Barbosa, D. O. Cosgrove, D. K. Nassiri, J. C. Bamber, C. R. Hill, Ultrasonic study of in vivo kinetic characteristics of human tissue. *Ultrasound Med Biol* 12, 927-937 (1986).
7. M. Tristam, D. C. Barbosa, D. O. Cosgrove, J. C. Bamber, C. R. Hill, Application of Fourier analysis to clinical study of patterns of tissue movement. *Ultrasound Med Biol* 14, 695-707 (1988).
8. R. M. Lerner, S. R. Huang, K. J. Parker, "Sono-elasticity" images derived from ultrasound signals in mechanically vibrated tissues. *Ultrasound Med Biol* 16, 231-239 (1990).
9. K. J. Parker, S. R. Huang, R. A. Musulin, R. M. Lerner, Tissue response to mechanical vibrations for "sonoelasticity imaging". *Ultrasound Med Biol* 16, 241-246 (1990).
10. K. J. Parker, R. M. Lerner, Sonoelasticity of organs: shear waves ring a bell. *J Ultrasound Med* 11, 387-392 (1992).
11. J. Ophir, I. Cespedes, H. Ponnekanti, Y. Yazdi, X. Li, Elastography: a quantitative method for imaging the elasticity of biological tissues. *Ultrason Imaging* 13, 111-134 (1991).



12. B. S. Garra, E. I. Cespedes, J. Ophir, S. R. Spratt, R. A. Zuurbier, C. M. Magnant, M. F. Pennanen, Elastography of breast lesions: initial clinical results. *Radiology* 202, 79-86 (1997).
13. M. O'Donnell, A. R. Skovoroda, B. M. Shapo, S. Y. Emelianov, Internal displacement and strain imaging using ultrasonic speckle tracking. *IEEE Transactions on Ultrasonic Ferroelectrics and Frequency Control* 41, 314-325 (1994).
14. S. Y. Emelianov, M. A. Lubinski, W. F. Weitzel, R. C. Wiggins, A. R. Skovoroda, M. O'Donnell, Elasticity imaging for early detection of renal pathologies. *Ultrasound Med Biol* 21 (7), 871-883, (1995).
15. L. Axel, L. Dougherty, Heart wall motion: improved method of spatial modulation of magnetization for MR imaging. *Radiology* 169, 59-63 (1988).
16. E. A. Zerhouni, D. M. Parish, W. J. Rogers, A. Yang, E. P. Shapiro, Human heart: tagging with MR imaging - a method for noninvasive assessment of myocardial motion. *Radiology* 169, 164-172 (1988).
17. N. J. Pelc, M. Drangova, L. R. Pelc, Y. Zhu, D. C. Noll, B. S. Bowman, R. J. Herfkens, Tracking of cyclic motion with phase-contrast cine MR velocity data *J Magn Reson Imaging*, 5(3), 339-345 (1995).
18. J. B. Fowlkes, S. Y. Emelianov, J. G. Pipe, A. R. Skovoroda, R. S. Adler, P. L. Carson, A. P. Sarvazyan, Magnetic resonance imaging techniques for detection of elasticity variation. *Med Phys* 22(11) 1771-1778, (1995).
19. R. Muthupillai, D. J. Lomas, P. J. Rossman, J. F. Greenleaf, A. Manduca, R. L. Ehman, Magnetic resonance elastography by direct visualization of propagating acoustic strain waves. *Science* 269, 1854-1857 (1995).
20. R. Muthupillai, P. J. Rossman, J. F. Greenleaf, S. J. Riederer, R. L. Ehman, MR imaging of acoustic strain waves: initial in vivo results, in "Proc., International Society for Magnetic Resonance in Medicine, 1996," p. 475.
21. D. B. Plewes, I. Betty, S. N. Urchuk, I. Soutar, Visualizing Tissue Compliance with MR Imaging. *J Magn Reson Imaging* 5, 733-738 (1995).
22. D. B. Plewes, G. Poole, M. Leitch, S. N. Urchuk, MR assessment of the viscoelastic properties of tissue through the propagation of transient strain waves, in "Proc., International Society for Magnetic Resonance in Medicine, 1996," p. 476.
23. I. Cespedes, J. Ophir, H. Ponnekanti, N. Maklad, Elastography: elasticity imaging using ultrasound with application to muscle and breast in vivo. *Ultrason Imaging* 15, 73-88 (1993).

24. A. Skovoroda, S. Emelianov, M. Lubinski, A. Sarvazyan, M. O'Donnell, Theoretical analysis and verification of ultrasound displacement and strain imaging. *IEEE Transactions on Ultrasonic Ferroelectrics and Frequency Control* 41(3), 302-313 (1994).
25. A. Skovoroda, S. Emelianov, M. O'Donnell, Tissue elasticity reconstruction based on ultrasound displacement and strain images: *IEEE Transactions on Ultrasonic Ferroelectrics and Frequency Control*, 42(4), pp. 747-765 (1995).
26. S. Y. Emelianov, A. R. Skovoroda, M. A. Lubinski, M. O'Donnell, Reconstructive elasticity imaging. *Acoustical Imaging*, 21, Plenum Press, New York, p. 241-253, 1995.
27. T.L. Chenevert, S.Y. Emelianov, A.R. Skovoroda: Elasticity Reconstructive Imaging Using Static Displacement and Strain Estimations. *Proceedings of the International Society of Magnetic Resonance in Medicine*, p-461, 1997.
28. T.L. Chenevert, A.R. Skovoroda, M. O'Donnell, and S.Y. Emelianov, "Elasticity reconstructive imaging via stimulated echo MRI," *Magnetic Resonance in Medicine*, 39, pp. 482-490 (1998). See Appendix.

## APPENDIX

Reprint of: "Elasticity reconstructive imaging via stimulated echo MRI," T.L. Chenevert, A.R. Skovoroda, M. O'Donnell, and S.Y. Emelianov, *Magnetic Resonance in Medicine*, 39, pp. 482-490 (1998).

Manuscript of: "Three-dimensional static displacement, stimulated echo NMR elasticity imaging,"

Derek D. Steele, Thomas L. Chenevert, Andrei R. Skovoroda and Stanislav Y. Emelianov, submitted to *Physics in Medicine and Biology*.

Chenevert, TL, Steele, DD, Emelianov, SY and Shovoroda, AR. Three-Dimensional Static Displacement Stimulated-Echo NMR Strain Imaging. *Proceedings of the International Society of Magnetic Resonance in Medicine* 1999; 263.

Steel, DD and Chenevert, TL, Emelianov, SY, and O'Donnell, M. Signal-to-Noise Consideration in Static Displacement, Stimulated Echo NMR Elasticity Imaging. *Proceedings of the International Society of Magnetic Resonance in Medicine* 1999; 1616.

# Elasticity Reconstructive Imaging by Means of Stimulated Echo MRI

Thomas L. Chenevert, Andrei R. Skovoroda, Matthew O'Donnell,  
Stanislav Y. Emelianov

**A method is introduced to measure internal mechanical displacement and strain by means of MRI. Such measurements are needed to reconstruct an image of the elastic Young's modulus. A stimulated echo acquisition sequence with additional gradient pulses encodes internal displacements in response to an externally applied differential deformation. The sequence provides an accurate measure of static displacement by limiting the mechanical transitions to the mixing period of the simulated echo. Elasticity reconstruction involves definition of a region of interest having uniform Young's modulus along its boundary and subsequent solution of the discretized elasticity equilibrium equations. Data acquisition and reconstruction were performed on a urethane rubber phantom of known elastic properties and an *ex vivo* canine kidney phantom using <2% differential deformation. Regional elastic properties are well represented on Young's modulus images. The long-term objective of this work is to provide a means for remote palpation and elasticity quantitation in deep tissues otherwise inaccessible to manual palpation.**

**Key words:** elastic Young's modulus; magnetic resonance imaging; elastography; strain imaging.

## INTRODUCTION

It is well known that tissue elastic properties may be altered by tumors. Young's elastic moduli may differ by orders of magnitude in soft tissues in various physiologic states (1, 2). This finding is the physical basis behind manual palpation used to detect "hard" masses (3, 4). Indeed, physical examination is the first diagnostic line of defense against breast cancer, because nodule hardness raises suspicion of malignancy. Detection of a new breast mass by physical examination is often sufficient for surgical excisional biopsy, even when not corroborated by other diagnostic tests. Manual palpation of the prostate, superficial lymph nodes, and abdominal organs are also commonly performed. Unfortunately, sensitivity of palpation is relatively poor within deep, dense, or heterogeneous tissues. Although the touch of a skilled interpreter is considered a powerful diagnostic instrument, most lesions detected by palpation tend to be relatively large and superficial.

Scientists are attempting to electronically extend the touch of the physical examiner using a variety of image-based techniques that infer tissue elasticity. The essential element is measurement of internal motion and strain in tissue structures experiencing mechanical stress. To date, most "elastography" has used ultrasound to track the relative motion of targets by specular reflection (5-7), by Doppler techniques (8-10), by cross-correlation of raw or processed acoustic echoes (11, 12), or by tracking speckle patterns (13-15). Usually an external static or dynamic deformation is applied while internal displacements or propagating shear waves are documented by imaging.

MRI has also been used to measure internal displacement and strain components of the heart using spatial magnetization tagging (16, 17) and phase-based velocity encoding (18). Elasticity reconstruction of an externally deformed phantom was demonstrated using magnetization tagging, but this method has spatial resolution limited by the tagged grid size and only measures 2D motion (19). More recently, motion phase encoding by means of bipolar gradients was used to produce two-dimensional (2D) displacement and strain maps in media mechanically driven by external forces (20-23). Strain and displacement maps infer internal elasticity but are also strongly affected by the applied deformational geometry. Consequently, these maps do not uniquely reflect internal tissue properties (i.e., elastic Young's modulus). Maps of dynamic strain-wave propagation, however, do allow measurement of local strain wavelength or velocity from which the local elastic modulus can be derived (20). Shear-wave attenuation, interference from standing waves off multiple reflectors, and limited resolvable points over the shear wavelength are potential drawbacks of this approach.

Relative to ultrasound, MRI has an advantage in overall resolution and accuracy for multidimensional displacement and strain measurement needed for elasticity reconstruction. Ultrasound can accurately measure axial (i.e., along the beam axis) motion at high spatial resolution ( $\leq$  millimeter), but lateral displacement is measured at much lower spatial resolution defined by the depth-dependent acoustic beam width. The third dimension is generally not even considered given the limitations of ultrasound. Consequently, reduced motion dimensionality and overall low motion resolution of the imaging system compromise the "elastogram." This shortcoming, in turn, constrains the mechanical model used in elasticity reconstruction. To date, only 1D motion models have been applied to ultrasound-derived elasticity images of tissues *in vivo* (12, 24). More accurate elasticity images are achieved by properly controlling external deforma-

## MRM 39:482-490 (1998)

From the Departments of Radiology (T.L.C.), Biomedical Engineering (S.Y.E.), and Electrical Engineering & Computer Science (M.O.), University of Michigan, Ann Arbor, Michigan; and Institute of Mathematical Problems of Biology (A.R.S., S.Y.E.), Russian Academy of Sciences, Pushchino, Russia.

Address correspondence to: Dr. Thomas L. Chenevert, University of Michigan Hospitals, Department of Radiology - MRI, 1500 E. Medical Center Drive, Ann Arbor, MI 48109-0030.

This research was supported in part by the National Institutes of Health grant DK47324 and by US Army grant DAMD17-97-7079.

Received April 15, 1997; revised September 8, 1997; accepted September 9, 1997.

tions, leading to 2D elasticity reconstruction within the imaging plane (25, 26).

In this work we present a method to spatially encode internal displacement of an object that has undergone an externally applied "static" deformation with subsequent reconstruction into elasticity maps. Unlike dynamic techniques designed to estimate elasticity from observations related to strain-wave propagation, static elasticity reconstruction involves estimation of local strain from displacement and numerical solution of differential elasticity equilibrium equations.

## THEORY OF RECONSTRUCTIVE ELASTICITY IMAGING

The goal of elasticity imaging is to reconstruct the elastic modulus of a desired tissue region using available measurements of displacement and strain components. Indeed, the mechanical properties of tissue are ultimately linked to the patterns of internal deformations, but the deformational geometry can greatly affect these patterns as well. To uniquely image tissue elasticity, the Young's modulus must be reconstructed from estimates of internal displacement and strain.

In this paper, the general approach to elasticity reconstruction was based on a model of linear, elastic, isotropic, incompressible media (26, 27). The key equations and considerations are briefly presented here. A more detailed description of elasticity reconstruction is given in an earlier publication (26).

In linear elasticity, the components of the strain ( $\epsilon_{ij}$ ) and stress ( $\sigma_{ij}$ ) tensors under static deformation are:

$$\epsilon_{ij} = \frac{1}{2} \left( \frac{\partial u_i}{\partial x_j} + \frac{\partial u_j}{\partial x_i} \right) = \frac{1}{2} (u_{i,j} + u_{j,i}) \quad [1]$$

$$\sigma_{ij} = p\delta_{ij} + \frac{2}{3} E\epsilon_{ij} \quad [2]$$

where  $u_i$  is a component of the displacement vector  $\mathbf{U} = (u_1, u_2, u_3)$  in Cartesian coordinates  $\mathbf{X} = (x_1, x_2, x_3)$ ,  $p$  is the static internal pressure,  $\delta_{ij}$  is the Kronecker delta symbol, and  $E = E(x_1, x_2, x_3)$  is the Young's elastic modulus. Note in Eq. [1], and the entire paper, the lower index after a comma means differentiation with respect to the corresponding spatial coordinate.

The static deformation of the medium can be described by the equilibrium condition:

$$\sum_{j=1}^3 \sigma_{ij,j} + f_i = 0, \quad i = 1, 2, 3 \quad [3]$$

where  $f_i$  is the body force per unit volume acting in the  $x_i$  direction. In addition, volume conservation for an incompressible medium leads to the following relationship between displacement and strain components

$$\nabla \cdot \mathbf{U} = \epsilon_{11} + \epsilon_{22} + \epsilon_{33} = u_{1,1} + u_{2,2} + u_{3,3} = 0 \quad [4]$$

Using Eqs. [1] and [2] for stress and strain components, and the incompressibility Eq. [4], the equilibrium condi-

tion with eliminated internal pressure  $p$  can be rewritten in the following form:

$$\begin{aligned} & 2\epsilon_{12}(E_{,11} - E_{,22}) + 2(u_{2,2} - u_{1,1})E_{,12} + 2\epsilon_{23}E_{,13} \\ & - 2\epsilon_{13}E_{,23} + (\nabla^2 u_2 + \omega_{12,1})E_{,1} - (\nabla^2 u_1 + \omega_{12,2})E_{,2} \\ & + \omega_{12,3}E_{,3} + \nabla^2 \omega_{12}E + 3(f_{2,1} - f_{1,2}) = 0 \\ & 2\epsilon_{13}(E_{,11} - E_{,33}) + 2\epsilon_{23}E_{,12} + 2(u_{3,3} - u_{1,1})E_{,13} \\ & - 2\epsilon_{12}E_{,23} + (\nabla^2 u_3 + \omega_{13,1})E_{,1} + \omega_{13,2}E_{,2} \\ & - (\nabla^2 u_1 + \omega_{13,3})E_{,3} + \nabla^2 \omega_{13}E + 3(f_{3,1} - f_{1,3}) = 0 \\ & 2\epsilon_{23}(E_{,22} - E_{,33}) + 2\epsilon_{13}E_{,12} - 2\epsilon_{12}E_{,13} + 2(u_{3,3} \\ & - u_{2,2})E_{,23} + \omega_{23,1}E_{,1} + (\nabla^2 u_3 + \omega_{23,2})E_{,2} - (\nabla^2 u_2 \\ & - \omega_{23,3})E_{,3} + \nabla^2 \omega_{23}E + 3(f_{3,2} - f_{2,3}) = 0 \end{aligned} \quad [5]$$

$$\omega_{12} = u_{2,1} - u_{1,2}, \quad \omega_{13} = u_{3,1} - u_{1,3}, \quad \omega_{23} = u_{3,2} - u_{2,3}$$

Clearly, the elasticity reconstruction process based on Eq. [5] requires accurate measurements of the displacement vector, or, to be more precise, requires accurate estimation of up to third-order spatial derivatives of the displacement. Equation [5] can also be written in terms of spatial derivatives of strain tensor components. The unique solution of the system of coupled partial differential equations [5] is determined by the boundary conditions, i.e., the elastic modulus  $E(\mathbf{X})$  must be given along the boundary of the reconstruction region of interest (ROI). It should also be noted here that the analytical solution of Eq. [5] is not generally possible, and numerical methods must be developed to solve this system of partial differential equations.

Based on the particular geometry of the phantoms and deformation system used in these experiments, Eq. [5] was simplified. A 2D approximation of Eq. [5] was used because the imaged plane was near the center of the

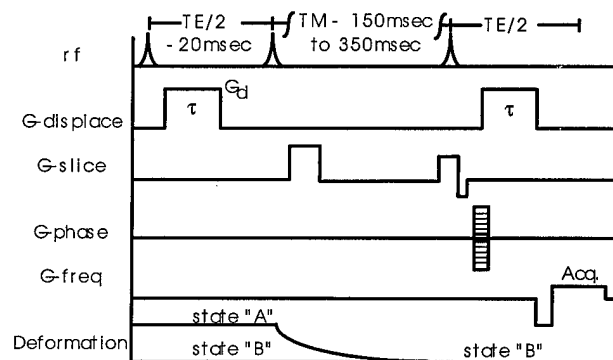


FIG. 1. Stimulated-echo data acquisition and object deformation sequence. Mechanical transitions occur during the long mixing time (TM) such that a static displacement equilibrium is achieved. Local displacement between deformation states "A" and "B" are encoded by phase shift proportional to "G-displace" amplitude  $G_d$ , and duration  $\tau$ .

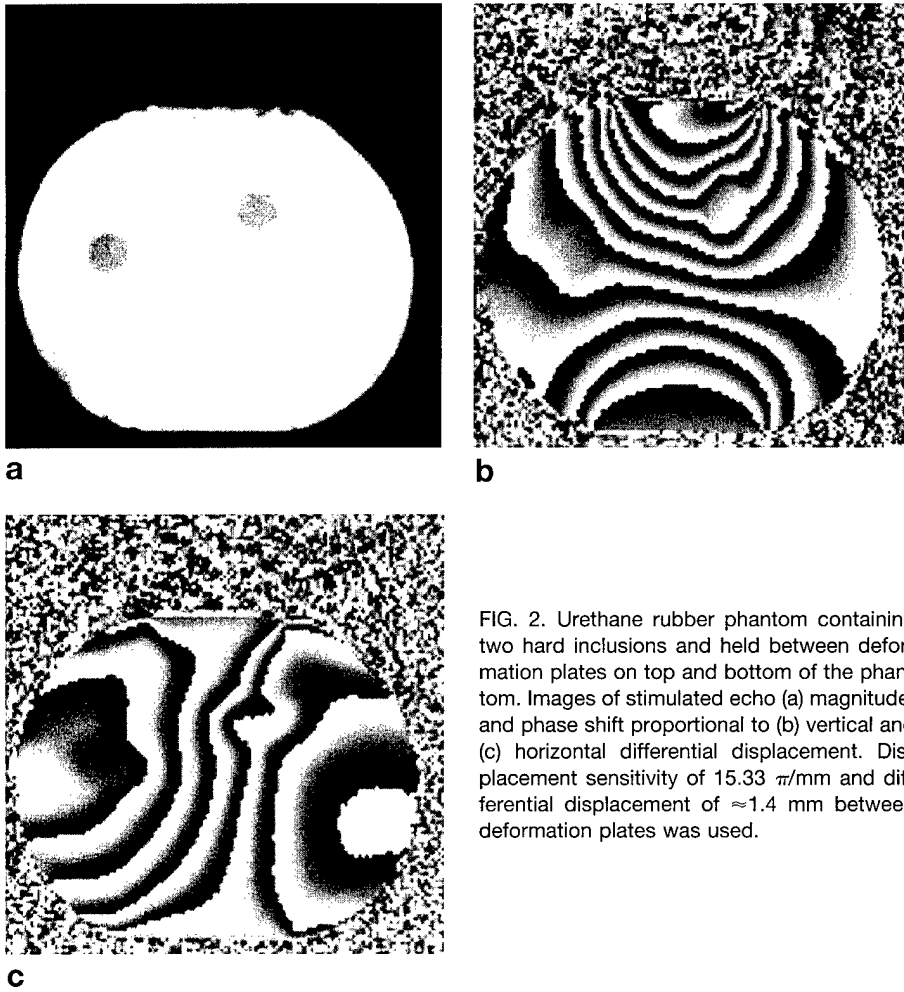


FIG. 2. Urethane rubber phantom containing two hard inclusions and held between deformation plates on top and bottom of the phantom. Images of stimulated echo (a) magnitude, and phase shift proportional to (b) vertical and (c) horizontal differential displacement. Displacement sensitivity of  $15.33 \pi/\text{mm}$  and differential displacement of  $\approx 1.4 \text{ mm}$  between deformation plates was used.

phantom. For such a plane (arbitrarily denoted as  $x_3 = 0$ ), the displacement vector components do not vary significantly as a function of the out-of-plane  $x_3$  coordinate, and therefore, the “plane strain state” condition is applicable. With this condition, Eq. [5] reduces to a single nontrivial equation:

$$\begin{aligned} & (E_{11} - E_{22})(u_{1,2} + u_{2,1}) + 2E_{12}(u_{2,2} - u_{1,1}) \\ & + 2E_{,1}(u_{2,11} + u_{2,22}) - 2E_{,2}(u_{1,11} + u_{1,22}) \\ & + E(u_{2,111} + u_{2,221} - u_{1,112} - u_{1,222}) + 3(f_{2,1} - f_{1,2}) = 0 \end{aligned} \quad [6]$$

Under conditions in which these assumptions are valid, only in-plane displacement  $u_1$  and  $u_2$  or their derivatives are needed to reconstruct the modulus in the plane  $x_3 = 0$ .

#### Static Displacement Measurement by Means of Stimulated Echo MRI

Shear-wave propagation speed in soft tissue is 1–20 m/s. Consequently, a shear wave imparted by a single-stroke or an oscillating deformation force may require tens of milliseconds to traverse an object  $\approx 100 \text{ mm}$  in size. The time for reflected waves to dampen may be much longer. “Dynamic” measurements, which encode displacement during shear-wave propagation, are potentially con-

founded by interference of the primary shear wave with reflected or standing shear waves. To avoid this condition, a “static” displacement encoding approach was adopted. It requires measurement of internal displacement between two or multiple deformations while the object is in mechanical equilibrium for each measurement. A stimulated echo sequence with displacement-encoding gradient pulses is used to achieve this, as shown in Fig. 1. Mechanical transition from state “A” to state “B” occurs during the stimulated echo mixing time, TM. A relatively long mixing time allows long-lived elastic vibrations to dampen before spatial encoding. Because the relevant magnetization during TM is longitudinal, it is unaffected by potentially ill-defined motions during the mechanical transition period. As a result, a more accurate static deformation measurement is achieved. Also note that precise synchronization of mechanical and pulsed gradient events is not critical as long as the mechanical transition begins after the second RF pulse

and is complete before the third RF pulse. Similarly, a long delay in  $TE$  could be used, but this is done at the expense of signal lost to  $T_2$  decay.

Local displacement is encoded by means of phase shift governed by pulsed-field gradient factors,

$$\tilde{\Phi}_d = \gamma \tilde{G}_d \tau \quad [7]$$

where displacement sensitivity,  $\Phi_d$ , is in units of (radians/distance). A phase reference acquisition is required for each displacement encode condition to remove pre-existing phase shifts that are unrelated to displacement. Reference data are acquired using the same pulse sequence, including displacement encode gradient pulses, but with the object maintained in state B. Note that all spatial encoding occurs from the third RF pulse and beyond. That is, the object is in one deformation state (state B) for both displacement and phase reference acquisitions during all spatial encoding segments of the sequence. Consequently, image registration or feature tracking algorithms (14) are not required to estimate displacement. Instead, local displacement is encoded directly by local phase of a corrected dataset,  $S_{\text{cor}}$ , given by,

$$S_{\text{cor}}(\vec{r}) = \frac{S_A(\vec{r}) S_B(\vec{r})^*}{|S_B(\vec{r})|} \equiv |S_A(\vec{r})| e^{i\varphi(\vec{r})} \quad [8]$$

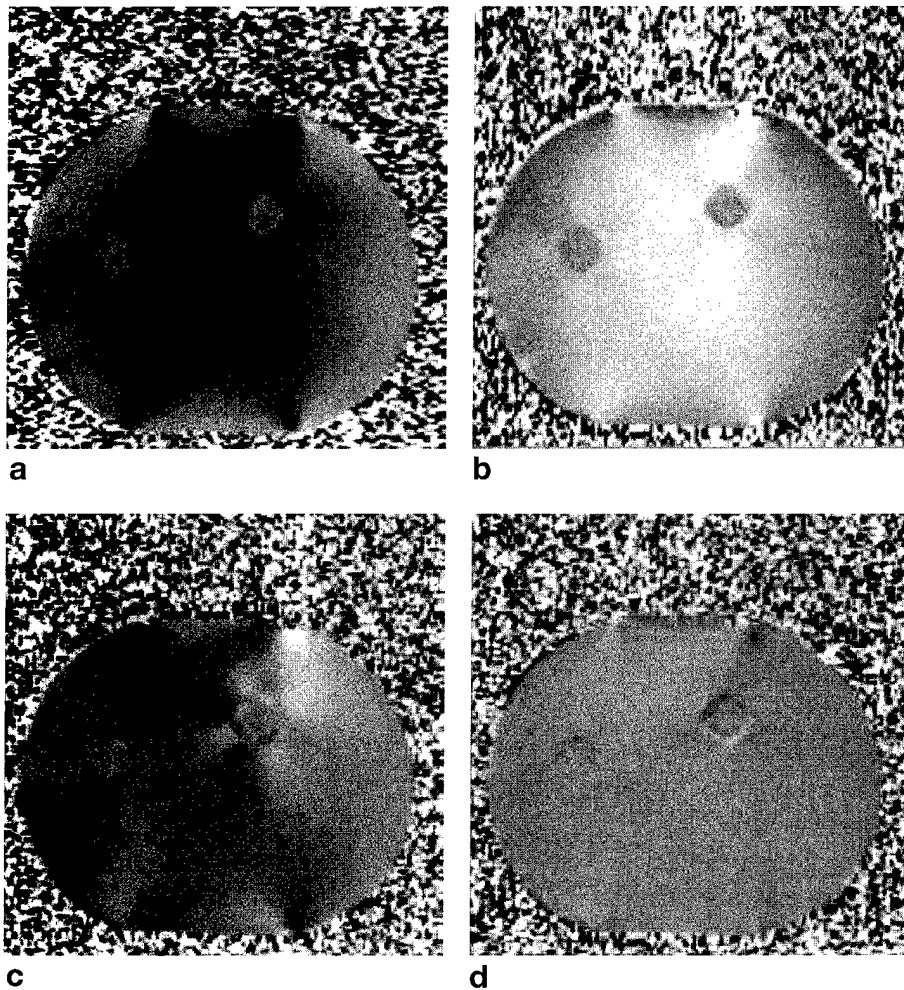


FIG. 3. Strain images calculated from first-order derivatives of the displacement images represented in Fig. 2. Normal strains (a)  $\epsilon_{11}$  and (b)  $\epsilon_{22}$ , and (c) shear strain  $\epsilon_{12} = \epsilon_{21}$  reflect internal elastic properties and the externally applied deformation field. The plane strain state assumption and phantom incompressibility suggest  $\epsilon_{11} \approx -\epsilon_{22}$  as is supported by the relatively featureless map of  $\epsilon_{11} + \epsilon_{22}$  in (d).

where  $S_A$  and  $S_B$  are the data acquired with the object initially in state A and state B, respectively. The unwrapped phase of the corrected dataset and Eq. [7] provides a local measure of displacement,  $U$ , by means of:

$$\varphi(\vec{r}) = \vec{\Phi}_d \cdot [\vec{r}_A - \vec{r}_B] = \vec{\Phi}_d \cdot U(\vec{r}) \quad [9]$$

Most sources of phase error, such as static field inhomogeneity, tend to be slowly varying functions of position. Therefore, the phase reference datasets may be acquired at relatively low spatial resolution to reduce scan time.

## METHODS

### Data Acquisition

Elasticity imaging was performed on two phantoms. One was an 85-mm diameter cylindrical urethane rubber phantom containing two 8-mm cylinders of hard material. Previously, the ratio of Young's modulus between the inclusion and background material was measured

$10.5 \pm 1.5$  for 30% surface deformation (19). In the present study, smaller surface deformation was applied, and consequently, the elasticity contrast within this phantom should be less than the previously measured ratio. Whereas the mechanical properties of the rubber phantom mimic soft tissue, the phantom had inherently poor NMR signal. A more tissue-equivalent phantom in terms of NMR and mechanical properties was achieved by embedding a fresh canine dog kidney (<24 h *ex vivo*) into a 130 mm  $\times$  105 mm  $\times$  75 mm block of 5% gelatin. One hour before MRI, 10 ml of 5% glutaraldehyde solution was injected into kidney parenchyma to create a hard lesion(s).

Phantoms were held securely in place under moderate preload pressure by two parallel acrylic plates. When pressure to the top plate was released, the phantom recoiled vertically an amount constrained by physical stops. Maximum vertical displacement was <1.5 mm, which represented <2% differential between state "A" (greater deformation) and state "B" (less deformation). Deformation was actuated pneumatically by an air-filled bladder on top of the phantom holder. Pneumatic pressure was stepped by a remote solenoid valve with timing controlled by an external transistor transistor logic (TTL) gate circuit triggered by the pulse sequence.

Displacement encoding gradient pulse duration,  $\tau = 4.5$  msec, and amplitude,  $G_d = 40$  mT/m, provided a displacement sensitivity of  $\Phi_d = 15.33 \pi/\text{mm}$  by means of Eq. [7]. The displacement encoding direction was alternated each pulse repetition between vertical and horizontal. For the urethane rubber phantom, acquisition parameters were  $TR = 1.3$  s,  $TM = 350$  msec,  $TE = 50$  msec,  $128 \times 128$  matrix, four signal averages, 100 mm field of view, and 10-mm section thickness. An additional  $128 \times 32$  matrix acquisition was collected for phase-reference correction of vertical and horizontal encoded data. The kidney phantom acquisition parameters were  $TR = 1$  s,  $TM = 200$  msec,  $TE = 76$  msec,  $256 \times 256$  matrix, two signal averages, 150 mm field of view, and 5-mm section thickness; with a  $256 \times 32$  dataset acquired for phase correction. All experiments were performed on a 2 T 18-cm bore MRI system (Bruker, formerly GE NMR

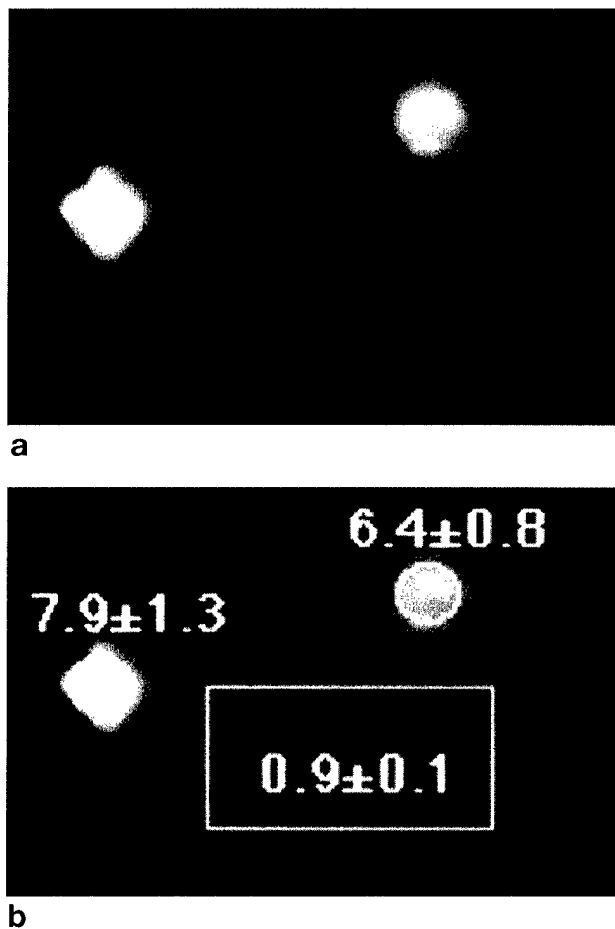


FIG. 4. (a) Reconstructed map of Young's modulus for the urethane rubber phantom within a  $63 \times 50$  mm region. The boundary of the region is defined to have a Young's modulus = 1. Relative Young's moduli for inclusions and background material are shown in (b).

Instruments), using a 150-mm transmit/receive birdcage coil.

#### Data Processing

Time-domain data were transferred for off-line processing as follows. Phase reference datasets were zero-filled and 2D Fourier transformed to a  $128 \times 128$  or  $256 \times 256$  matrix for phase correction by means of Eq. [7]. The resulting phase maps were used to estimate the spatial derivatives of the in-plane displacements necessary for elasticity reconstruction (6). Note phase unwrapping is not strictly required because only phase derivatives are used. Assuming the displacement fields are continuous, resulting in small differential displacement at any pixel compared with the total displacement, the differential displacement between two neighboring pixels was directly computed from the angle of the complex multiplication of each pixel with the conjugate of the neighboring pixel, then scaled by  $1/\Phi_d$ .

Solving Eq. [6] for unknown  $E(x_1, x_2)$  performed the elasticity reconstruction, i.e., reconstruction of the spatial distribution of elastic Young's modulus. As was noted previously, the unique solution of a boundary value problem (Eq. [5] or [6]) is determined by the bound-

ary conditions. Therefore, a rectangular ROI was identified within the imaging planes for both phantoms. For the phantom with two hard inclusions, the ROI was a region of  $63 \times 50$  mm positioned approximately in the center of the phantom and included both inclusions. For the canine kidney phantom, the rectangular  $94 \times 51$  mm ROI included the whole kidney cross-section. In both cases, the Young's modulus value along the ROI boundary was set to "one" resulting in reconstruction of relative Young's modulus. More detailed analysis and discussion of defining the ROI was considered previously (26).

Elasticity reconstruction Eqs. [5] and [6] assume that spatial derivatives of the Young's modulus are continuous functions. To ensure continuous elasticity distribution, the spatial derivatives of the displacement were low-pass filtered before elasticity reconstruction, resulting in mild spatial resolution reduction.

After defining the boundary conditions, Eq. [6] was discretized over the ROI with the same grid spacing as the MR images, where all spatial derivatives of the displacement/strain (i.e., coefficients in Eq. [6] for unknown Young's modulus distribution) were approximated by finite differences. The linear set of equations resulting from discretization of Eq. [6] was solved iteratively, where the error in each step was estimated by averaging the left-hand side of Eq. [6] over the ROI using the current estimate of the elasticity distribution. From step to step, the Young's modulus distribution was updated based on the changes in the average error.

#### RESULTS

Magnitude and corrected phase images of the urethane rubber phantom are shown in Fig. 2. Given that  $\Phi_d = 15.33 \pi/\text{mm}$ , the number of  $2\pi$  phase bands in Fig. 2b indicates that the vertical excursion of the phantom top relative to the bottom was  $\approx 1.4$  mm; similarly, the relative lateral displacement between left and right edges of the phantom was  $\approx 0.8$  mm (Fig. 2c). Reduced phase slopes in the regions of the hard inclusions are clearly visible on the phase images. Normal strain,  $\epsilon_{11}$  and  $\epsilon_{22}$ , and shear strain,  $\epsilon_{12} = \epsilon_{21}$ , maps are illustrated in Figs. 3a–3c, respectively. The observed contrast reversal between  $\epsilon_{11}$  and  $\epsilon_{22}$  is a result of phantom incompressibility (like soft tissue), which yields  $\epsilon_{11} = -\epsilon_{22}$  assuming negligible out-of-plane strain. Consequently, the sum ( $\epsilon_{11} + \epsilon_{22}$ ) is relatively "flat" as shown at equivalent grayscale settings in Fig. 3d. Also note, whereas the strain maps clearly exhibit object-specific detail (i.e., inclusions), features related to the applied external deformation are quite conspicuous. This fact demonstrates why an elasticity reconstruction is needed. The Young's modulus was reconstructed for a  $63 \times 50$  mm region as presented in Fig. 4a. The boundary of the elasticity reconstruction area was defined to have value "1." The relative elastic moduli for select regions are indicated in Fig. 4b and are consistent with the known elasticity of these materials (19).

The canine kidney phantom is shown in Fig. 5 as magnitude (Fig. 5a), vertical (Fig. 5b), and horizontal (Fig. 5c) phase shift images. It is apparent from the vertical phase image (Fig. 5b) that although  $\approx 1.24$ -mm rel-

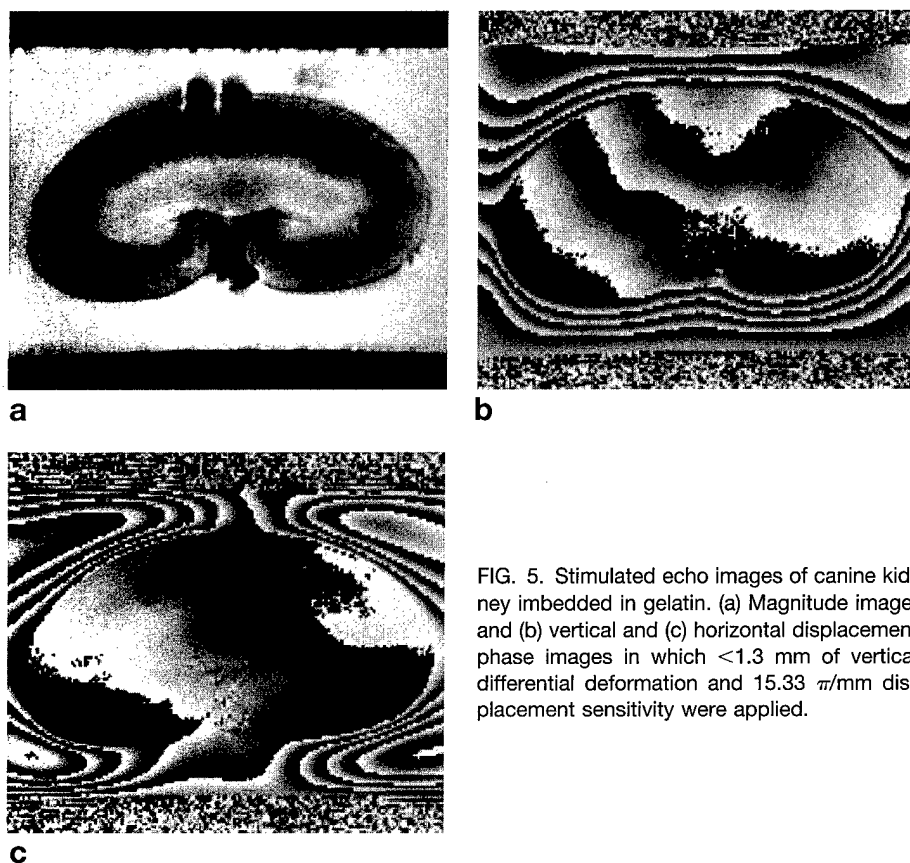


FIG. 5. Stimulated echo images of canine kidney imbedded in gelatin. (a) Magnitude image, and (b) vertical and (c) horizontal displacement phase images in which  $<1.3$  mm of vertical differential deformation and  $15.33 \pi/\text{mm}$  displacement sensitivity were applied.

active displacement spans the full phantom, only  $\approx 0.26$  mm of it is within the kidney. Consequently, there is a high concentration of strain near the gel-kidney interface, as is clear on the strain maps (Fig. 6). As noted before, strain images exhibit contrast related to a combination of internal structure and the externally applied deformation. Elasticity reconstruction, however, reduces the ambiguity and exhibits contrast dominated by internal elastic properties (Fig. 7a). It is also encouraging to note that whereas there was only moderate strain contrast within the kidney, elasticity contrast within renal parenchyma and central sinus are well distinguished on the Young's modulus image. Moreover, the site of glutaraldehyde injection (top-right quadrant of images) exhibited the highest relative Young's modulus. Approximately 20 h after MRI, the kidney phantom was sliced at a plane corresponding to that studied by MRI. An optical image of this slice is shown in Fig. 7c. The freshly cut surface was palpated such that areas of relatively "hard" parenchyma could be noted. Arrows in Fig. 7c mark the most conspicuous areas of hardness; the largest area corresponds to the high Young's modulus region in the upper-right quadrant of the kidney.

## DISCUSSION

In this work we introduce a method to image and quantify internal elastic properties of an object by means of displacement-sensitive MRI with associated elasticity reconstruction. The data acquisition segment employs gradient pulses to encode internal displacement by means of

phase using a stimulated echo sequence. Internal displacements occur in response to an external deformation force synchronized to the acquisition sequence. By timing control, mechanical motion occurs while the relevant magnetization is longitudinal. The stimulated echo allows extension of the mechanical transition period to avoid potentially long-lived or ill-defined oscillations within the object such that an estimate of "static" displacement is achieved. Image registration or feature tracking (14) is not required because the object is in one deformation state for all spatial encoding.  $T_1$  relaxation and diffusion, which erode signal, ultimately set practical limits on this period. In these experiments, 200 to 350 msec was sufficient to allow static displacement measurement of rubber and gelatin/tissue phantoms using a simple air-bladder pneumatic system.

This arrangement required the object to "passively" recoil during the TM period. Clearly, a faster deformation system can be built using external forces to "actively" deform the object during the stimulated echo mixing period. A shorter mixing time would then be used yielding a larger signal.

To date, two approaches are present in elasticity imaging: static reconstructive elasticity imaging (25, 26) and dynamic shear-wave elasticity imaging (20, 21, 23). In both, an external static or dynamic deformation is applied while the resulting displacement/strain or propagating shear wave is detected using an imaging modality. In reconstructive elasticity imaging, the elasticity distribution must be reconstructed from static displacement and strain images. The ability to control the internal deformation pattern by varying the externally applied load, and high SNR displacement and strain estimates are the benefits of this method, although numerical reconstruction algorithms are required. Wherein the modeled assumptions are valid, these algorithms exist. For more general applications, they must be refined further. In shear-wave elasticity imaging, local shear wavelength measurements allow direct and simple calculation of the shear elastic modulus. However, the interference of shear waves reflected from any elasticity inhomogeneities within the tissue, along with attenuation of shear waves, and conversion between shear and bulk waves are challenges of this method.

In these experiments a displacement sensitivity of  $\Phi_d = 15.33 \pi/\text{mm}$  was achieved using moderate gradient factors. The ultimate quality of Young's modulus reconstruction depends on the induced phase shift, equal to



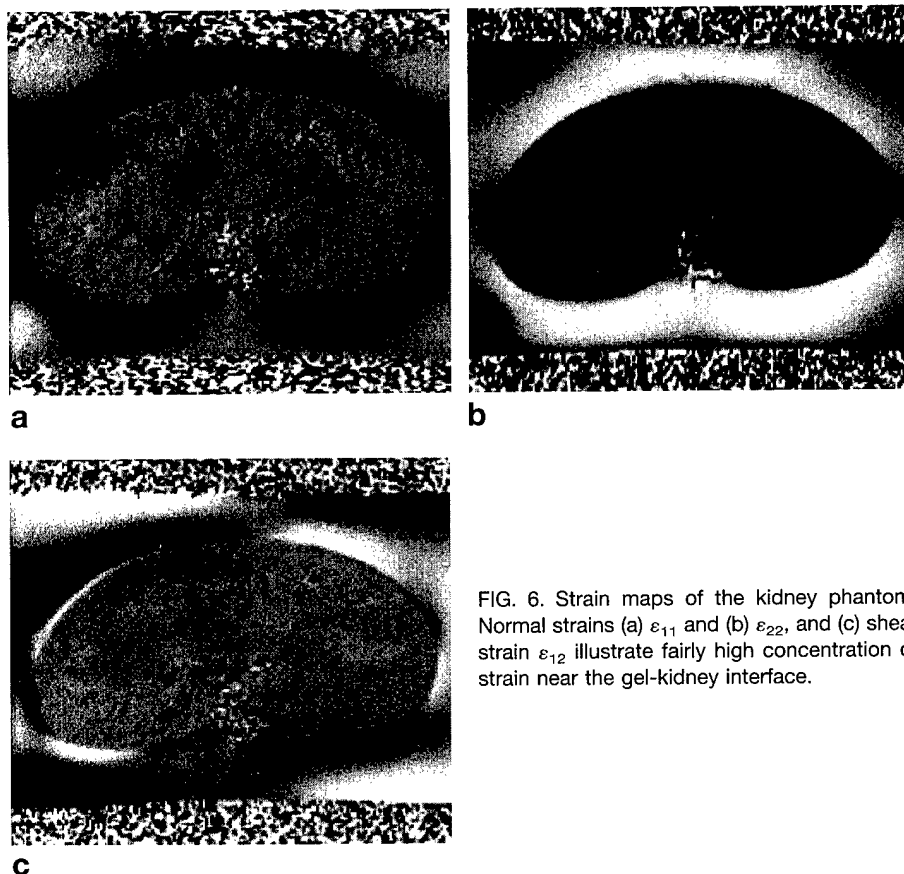


FIG. 6. Strain maps of the kidney phantom. Normal strains (a)  $\epsilon_{11}$  and (b)  $\epsilon_{22}$ , and (c) shear strain  $\epsilon_{12}$  illustrate fairly high concentration of strain near the gel-kidney interface.

the product of  $\Phi_d$  and local displacement. There is a limit, however, to the advantages gained by increasing phase shift. As spatial phase gradients become large, the phase distribution within a given voxel reduces signal amplitude. Assuming a linear phase distribution of range  $\beta$  with a voxel, the signal modulation function is given by  $\text{sinc}(\beta)$ . For illustration, consider the vertical phase excursion of  $21\pi$  observed across the 80-mm phantom in Fig. 2b. If the vertical phase excursion was evenly distributed across voxels, the phase range within each 0.78-mm voxel would be approximately  $0.2\pi$ . This implies a signal reduction factor of  $\text{sinc}(0.2\pi) = 0.94$  (i.e., signal loss of 6%). Clearly phase gradients can be more concentrated depending on object geometry, elastic heterogeneity, and deformation geometry. This concentration can lead to regions of significant signal loss in a manner analogous to flow dephasing in conventional MRI. Under such conditions, a smaller voxel size can (paradoxically) yield higher signal. In addition, inspection for significant signal loss within the displacement-sensitive magnitude image can identify high-strain regions near soft/hard interfaces of a lesion.

Water diffusion in the presence of displacement encoding gradients is another source of signal attenuation. We estimate the signal reduction factor for freely diffusing water was  $\approx 0.24$  in these experiments (i.e., 76% signal lost to diffusion effects). Diffusion effects are lessened by reducing  $\Phi_d$ , or alternatively by shortening TM without affecting  $\Phi_d$ . In either case, diffusion effects are assumed independent of the deformation state, and

therefore are ignored in the elasticity reconstruction. Because displacement phase shift is the product of local displacement and  $\Phi_d$ , the selection of  $\Phi_d$  is somewhat arbitrary as long as the applied differential deformation is adequate for elasticity reconstruction. In these preliminary experiments, the differential deformation was  $< 1.5$  mm across the imaged object. For multi-step acquisitions, as done here, good reproducibility of deformation is essential. Significant variation in deformation magnitude over the acquisition will lead to phase instability, motion-like artifact in base images, and errors that propagate through the elasticity reconstruction. It is a minor technical challenge to achieve relatively high displacement reproducibility in the deformation apparatus. Irreproducible motions that originate within the imaged object, however, can be problematic and are analogous to undesired physiologic motion artifacts in *in vivo* diffusion MRI. Fortunately, unlike diffusion and physiologic motions, the targeted motion in elasticity imaging is externally driven. As such, the displacement amplitude in response to an external differential deformation can be significantly greater than irreproducible or asynchronous displacement. For many *in vivo* applications including the breast, increasing the differential deformation severalfold relative to that applied in these phantom studies can reduce motion artifact. Gradient factors and  $\Phi_d$  would be reduced accordingly, which would yield the added benefit of increased signal otherwise lost to diffusion effects.

In practice, the definition of a closed contour of constant Young's modulus within the tissue can be a challenge. A hybrid procedure can be used as detailed elsewhere (26) and summarized as follows. The strain images are first processed to highlight boundaries between regions of different elastic modulus. This procedure is based on the stress continuity property of continuous media such as tissue and can define regions of very small modulus variations. After this boundary detection, closed contours of small elasticity variations are defined. The modulus along the contours is considered constant, thereby providing the boundary condition for complete reconstruction of the elasticity within the region of interest based on numerical solution of Eq. [6]. The elasticity distribution reconstructed in this way is the modulus relative to the modulus along the boundary. For breast elasticity imaging, it is anticipated that such a contour can be defined *a priori* within the subcutaneous fat that surrounds breast parenchyma. As-

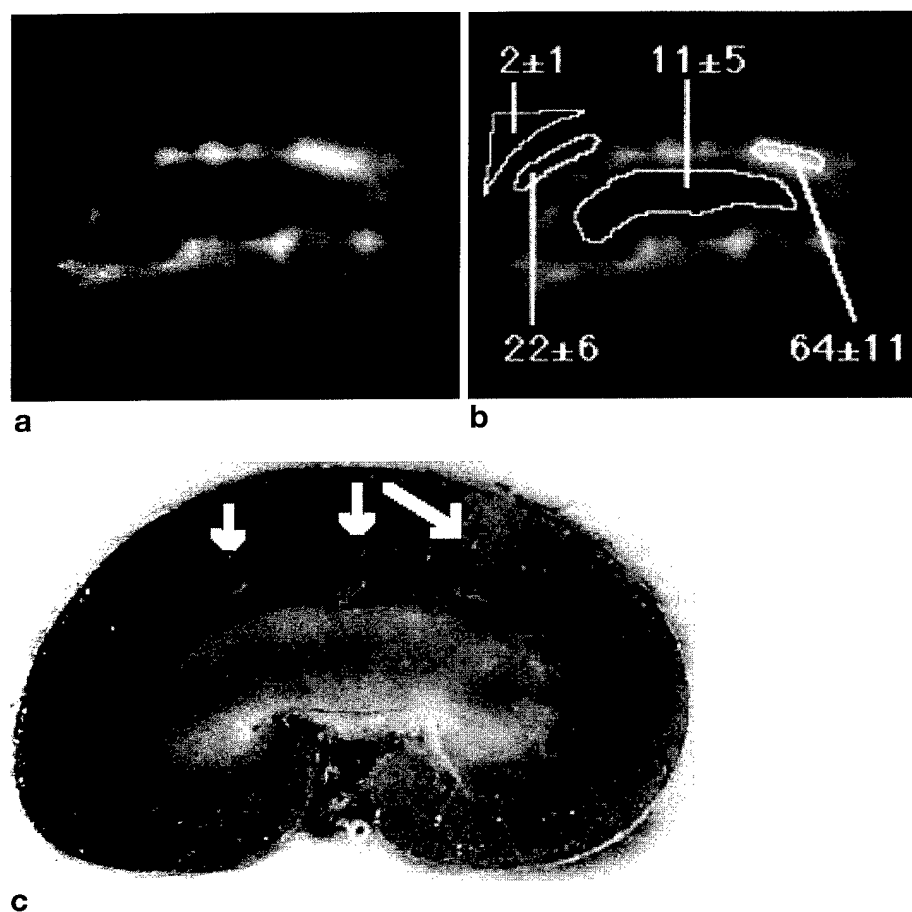


FIG. 7. (a) Reconstructed Young's modulus image within a rectangular  $94 \times 51$  mm region encompassing the kidney. (b) Relative Young's modulus for the scribed ROIs indicate high elastic modulus at the glutaraldehyde injection site in the upper-right quadrant of the kidney parenchyma. (c) The optical image of the kidney phantom approximately 20 h after MRI. Areas marked by arrows were noticeably harder as assessed by sense of manual touch.

suming the Young's modulus of the fat boundary is constant, the relative Young's modulus image of parenchyma can be reconstructed. Alternatively, the breast can be surrounded by a high-signal cuff of known elastic modulus and imaged. An image of absolute Young's modulus can then be reconstructed if the boundary contour is defined within the cuff material.

Some artifacts present in elasticity images (Figs. 4 and 7) are due to violation of the plane strain state approximation in these experiments. Indeed, if a plane strain state is not present, the reconstruction based on Eq. [6] will be in error. The elasticity reconstruction, however, does not have to be limited by a plane strain assumption if all 3D components of the displacement vector are available. Fortunately, such information would be available using 3D displacement encoding within a volumetric imaging sequence. The issue of long scan time could be resolved by incorporating echoplanar imaging or fast-spin-echo segments for spatial encoding. Correspondingly, an elasticity reconstruction based on Eq. [5] would be applied to produce volumetric elasticity maps.

The long-range goal of quantitative elasticity imaging is to provide remote palpation thus expanding its limited

range to include deep lying lesions. One application would be measurement of elasticity in breast tissue not accessible to manual palpation. *In situ* studies of Young's elastic modulus performed on samples of breast tissue indicate that there is a large difference in elastic modulus between normal and pathologically transformed breast tissues. Others have analyzed the Young's modulus differences between different soft tissues and have found 1–2 orders of magnitude difference in Young's elastic moduli of a tissue in different physiologic states (1). If elastic changes predate formation of calcifications, elasticity imaging could potentially increase detection and/or characterization of malignant breast masses and thus be an important addition to existing clinical diagnostic tools. Practical issues such as the relatively high cost of MRI may hinder use of this approach as a screening test. Nevertheless, additional work to define the role of this technique as a primary diagnostic tool or supplemental problem-solving modality in the management of soft-tissue disease is well justified.

## REFERENCES

1. A. P. Sarvazyan, A. R. Skovoroda, S. Y. Emelianov, J. B. Fowlkes, J. G. Pipe, R. S. Adler, R. B. Buxton, P. L. Carson, Biophysical Bases of Elasticity Imaging, in "Acoustical Imaging," volume 21, p. 223–240, Plenum Press, New York, 1995.
2. A. R. Skovoroda, A. N. Klishko, D. A. Gukasyan, E. I. Maevsky, V. D. Ermilova, G. A. Oranskaya, A. P. Sarvazyan, Quantitative analysis of the mechanical characteristics of pathologically altered soft biological tissues. *Biofizika* **40**, 1335–1340, (1995).
3. D. Hill, V. White, D. Jolley, K. Mapperson, Self examination of the breast: is it beneficial? Meta-analysis of studies investigating breast self examination and the extent of disease in patients with breast cancer. *Br. J. Med.* **297**, 271–275 (1988).
4. P. A. Newcomb, S. Weiss, B. E. Storer, D. Scholes, B. E. Young, Breast self examination in relation to the occurrence of advanced breast cancer. *J. Natl. Cancer Inst.* **83**, 260–265 (1991).
5. R. J. Dickinson, C. R. Hill, Measurement of soft tissue motion using correlation between A-scans. *Ultrasound Med. Biol.* **8**, 263–271 (1982).
6. M. Tristram, D. C. Barbosa, D. O. Cosgrove, D. K. Nassiri, J. C. Bamber, C. R. Hill, Ultrasonic study of *in vivo* kinetic characteristics of human tissue. *Ultrasound Med. Biol.* **12**, 927–937 (1986).
7. M. Tristram, D. C. Barbosa, D. O. Cosgrove, J. C. Bamber, C. R. Hill, Application of Fourier analysis to clinical study of patterns of tissue movement. *Ultrasound Med. Biol.* **14**, 695–707 (1988).
8. R. M. Lerner, S. R. Huang, K. J. Parker, "Sono-elasticity" images derived from ultrasound signals in mechanically vibrated tissues. *Ultrasound Med. Biol.* **16**, 231–239 (1990).

9. K. J. Parker, S. R. Huang, R. A. Musulin, R. M. Lerner, Tissue response to mechanical vibrations for "sonoelasticity imaging." *Ultrasound Med. Biol.* **16**, 241-246 (1990).
10. K. J. Parker, R. M. Lerner, Sonoelasticity of organs: shear waves ring a bell. *J. Ultrasound Med.* **11**, 387-392 (1992).
11. J. Ophir, I. Cespedes, H. Ponnekanti, Y. Yazdi, X. Li, Elastography: a quantitative method for imaging the elasticity of biological tissues. *Ultrasound Imaging*. **13**, 111-134 (1991).
12. B. S. Garra, E. I. Cespedes, J. Ophir, S. R. Spratt, R. A. Zurbier, C. M. Magnant, M. F. Pennanen, Elastography of breast lesions: initial clinical results. *Radiology* **202**, 79-86 (1997).
13. R. Adler, J. M. Rubin, P. Bland, P. Carson, Characterization of transmitted motion in fetal lung: quantitative analysis. *Med. Phys.* **16**, 333-337 (1988).
14. M. O'Donnell, A. R. Skovoroda, B. M. Shapo, S. Y. Emelianov, Internal displacement and strain imaging using ultrasonic speckle tracking. *IEEE Trans. Ultrason. Ferroelectrics and Frequency Control* **41**, 314-325 (1994).
15. S. Y. Emelianov, M. A. Lubinski, W. F. Weitzel, R. C. Wiggins, A. R. Skovoroda, M. O'Donnell, Elasticity imaging for early detection of renal pathologies. *Ultrasound Med. Biol.* **21**, 871-883 (1995).
16. L. Axel, L. Dougherty, Heart wall motion: improved method of spatial modulation of magnetization for MR imaging. *Radiology* **169**, 59-63 (1988).
17. E. A. Zerhouni, D. M. Parish, W. J. Rogers, A. Yang, E. P. Shapiro, Human heart: tagging with MR imaging - a method for noninvasive assessment of myocardial motion. *Radiology* **169**, 164-172 (1988).
18. N. J. Pelc, M. Drangova, L. R. Pelc, Y. Zhu, D. C. Noll, B. S. Bowman, R. J. Herfkens, Tracking of cyclic motion with phase-contrast cine MR velocity data. *J. Magn. Reson. Imaging* **5**, 339-345 (1995).
19. J. B. Fowlkes, S. Y. Emelianov, J. G. Pipe, A. R. Skovoroda, R. S. Adler, P. L. Carson, A. P. Sarvazyan, Magnetic resonance imaging techniques for detection of elasticity variation. *Med. Phys.* **22**, 1771-1778 (1995).
20. R. Muthupillai, D. J. Lomas, P. J. Rossman, J. F. Greenleaf, A. Manduca, R. L. Ehman, Magnetic resonance elastography by direct visualization of propagating acoustic strain waves. *Science* **269**, 1854-1857 (1995).
21. R. Muthupillai, P. J. Rossman, J. F. Greenleaf, S. J. Riederer, R. L. Ehman, MR imaging of acoustic strain waves: initial *in vivo* results, in "Proc., ISMRM, 4th Scientific Meeting and Exhibition, 1996," New York, p. 475.
22. D. B. Plewes, I. Betty, S. N. Urchuk, I. Soutar, Visualizing tissue compliance with MR imaging. *J. Magn. Reson. Imaging* **5**, 733-738 (1995).
23. D. B. Plewes, G. Poole, M. Leitch, S. N. Urchuk, MR assessment of the viscoelastic properties of tissue through the propagation of transient strain waves, in "Proc., ISMRM, 4th Scientific Meeting and Exhibition, 1996," New York, p. 476.
24. I. Cespedes, J. Ophir, H. Ponnekanti, N. Maklad, Elastography: elasticity imaging using ultrasound with application to muscle and breast *in vivo*. *Ultrasound Imaging* **15**, 73-88 (1993).
25. A. Skovoroda, S. Emelianov, M. Lubinski, A. Sarvazyan, M. O'Donnell, Theoretical analysis and verification of ultrasound displacement and strain imaging. *IEEE Trans. Ultrason. Ferroelectrics and Frequency Control* **41**, 302-313 (1994).
26. A. Skovoroda, S. Emelianov, M. O'Donnell, Tissue elasticity reconstruction based on ultrasound displacement and strain images. *IEEE Trans. Ultrason. Ferroelectrics and Frequency Control* **42**, 747-765 (1995).
27. S. Y. Emelianov, A. R. Skovoroda, M. A. Lubinski, M. O'Donnell, Reconstructive Elasticity Imaging, in "Acoustical Imaging," volume 21, p. 241-253, Plenum Press, New York, 1995.

# Three-dimensional static displacement stimulated-echo NMR strain imaging

THOMAS L. CHENEVERT, DEREK D. STEELE\*, STANISLAV Y. EMELIANOV\*§, AND ANDREI R. SKOVORODA§  
Department of Radiology and Department of Biomedical Engineering\*, The University of Michigan, Ann Arbor, MI 48109-0553  
Institute of Mathematical Problems of Biology, Russian Academy of Sciences; Pushchino, Russia §

## INTRODUCTION

Elasticity MRI is the reconstruction of the elastic modulus in media using local displacement measurements of an object under static deformation [1], or directly from measurements of shear wave propagation [2]. Often it is assumed out of plane strain is approximately zero. However, this plane strain state approximation does not hold in general. Estimates of the full 3D displacement and strain fields are required to accurately reconstruct elasticity. Here we describe such a method based on static displacement, stimulated-echo imaging [3]. As previously described, this approach encodes local displacement in response to an externally-applied deformation. A relatively long STE mixing time (200-300msec) allows ill-defined mechanical vibrations to dampen to where equilibrium conditions apply. The approach uses pulsed-field gradients (PFG) to encode displacement and is, in principle, readily extended to measure the full 3D displacement field.

## METHODS

Features of the displacement-encoding STE technique have been described previously [3] but are summarized here. The initial spatial configuration of an elastic object is encoded by application of a PFG between the first two non-selective  $90^\circ$  rf pulses. An externally-applied deformation force transforms the object to a new configuration during the mixing time, TM, of the STE. The differential surface deformation can be relatively subtle ( $\leq 5\text{mm}$ ) and is chosen to complement the applied PFG area which defines displacement sensitivity ( $\sim 3\text{-}16\pi/\text{mm}$ ). Mixing time must be sufficient for the object to come to rest by the  $3^{\text{rd}}$  slice/slab-selective  $90^\circ$  rf pulse. A second PFG prior to signal readout yields a phase directly proportional to local displacement between initial and final object configuration. To achieve 3D, a fast-spin-echo train was appended to the STE with an additional centric-ordered z-slab phase-encode echo train (8-16 ETL on kz). Conventional phase-encoding was used for the remaining spatial dimension. Acquisition of data sets with interleaved PFG gradients applied along X, Y, and Z axes: TR=1"; 256 x 128 x 8; 4ave;  $3.8\pi/\text{mm}$  sensitivity. Phase correction was done via a sparse reference dataset (32 ky lines).

A tissue-mimicking block phantom containing ramped bars of harder material ( $\approx 6\times$  Young's modulus) was held between two pneumatic deformation plates. These parallel plates released a 5mm differential surface deformation during TM=270ms.

## RESULTS

Images of the phantom shown in figure 1 are (a) magnitude and phase (i.e. displacement) images along (b) X, (c) Y and (d) Z directions. Corresponding strain images illustrated in figure 2 are (a)  $\epsilon_{xx}$ , (b)  $\epsilon_{yy}$ , (c)  $\epsilon_{xy}$ , and (d)  $(\epsilon_{xx}+\epsilon_{yy})$ . Note,  $(\epsilon_{xx}+\epsilon_{yy})$  should be zero if the plane-strain condition holds. Apparent structure in figure 2(d) indicates there is out of plane strain.

## DISCUSSION

Extension of elasticity MRI to 3D is essential to implement a general elasticity reconstruction. 3D elasticity reconstruction algorithms have been described [1], but have not been implemented due to lack of suitable 3D data acquisition schemes. The method presented here represents an initial step toward that end.

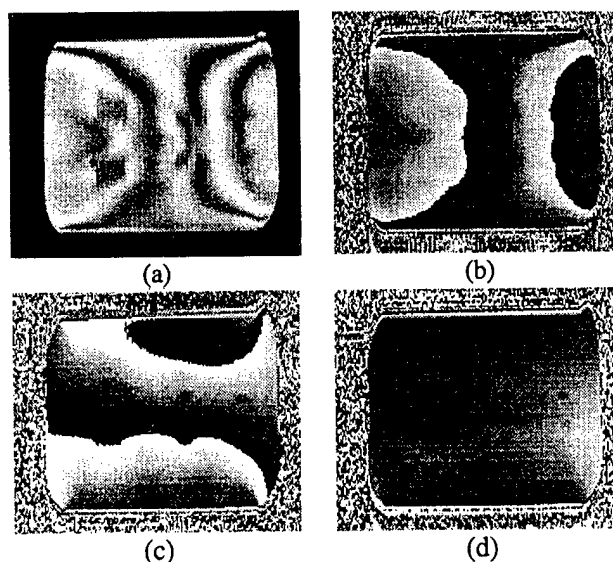


Figure 1

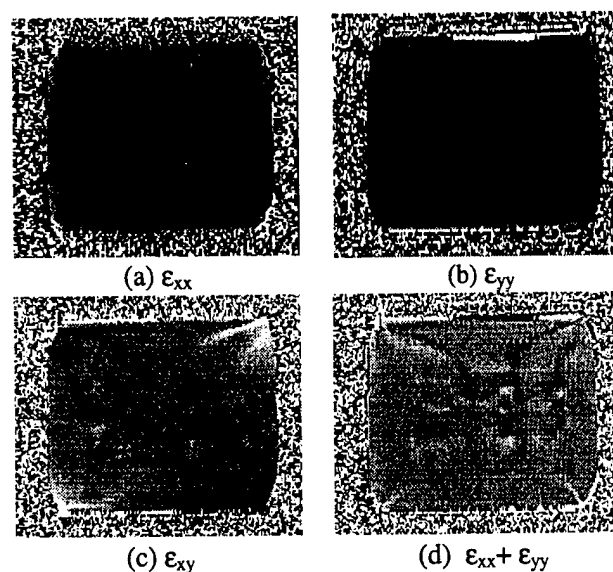


Figure 2

## REFERENCES

1. A. Skovoroda, S. Emelianov, M. O'Donnell, Tissue elasticity reconstruction based on ultrasound displacement and strain images: IEEE Transactions on Ultrasonic Ferroelectrics and Frequency Control 1995; 42(4), pp747-765.
2. R. Muthupillai, D. J. Lomas, P. J. Rossman, J. F. Greenleaf, A. Manduca, R. L. Ehman, Magnetic resonance elastography by direct visualization of propagating acoustic strain waves. Science 269, 1854-1857 (1995).
3. Chenevert TL, Skovoroda AR, O'Donnell M, Emelianov SY. Elasticity reconstructive imaging by means of stimulated echo MRI. Magn Reson Med 1998; 39(3):482-490.

# Three-dimensional static displacement, stimulated echo NMR elasticity imaging

Derek D. Steele†, Thomas L. Chenevert‡, Andrei R. Skovoroda§ and Stanislav Y. Emelianov†§

† Department of Biomedical Engineering, University of Michigan Medical Center, 3310 Kresge III, Ann Arbor, MI 48109-0553, USA

‡ Department of Radiology, University of Michigan Hospitals, 1500 E. Medical Center Drive, Ann Arbor, MI, 48109-0030, USA

§ The Institute of Mathematical Problems of Biology, Russian Academy of Sciences, Pushchino, Russia 142292

**Abstract.** This article presents a method for measuring three-dimensional mechanical displacement and strain fields using stimulated echo MRI. Additional gradient pulses encode internal displacements in response to an externally applied deformation. By limiting the mechanical transition to the stimulated echo mixing time, a more accurate static displacement measurement is obtained. A three-dimensional elasticity reconstruction within a region of interest having a uniform shear modulus along its boundary is performed by numerically solving discretized elasticity equilibrium equations. Data acquisition and reconstruction were performed using a silicone gel phantom containing an inclusion of known elastic properties. A comparison between two-dimensional and three-dimensional reconstructions from simulated and experimental displacement data shows higher accuracy from the three-dimensional reconstruction. The long term objective of this work is to provide a method for remotely palpating and elastically quantitating manually inaccessible tissues.

## 1. Introduction

### 1.1. Motivation

Palpation has long been used by physicians as a means to detect disease. The underlying basis for this detection is the presence of "hard" tissue. Evidence suggests that Young's (or shear) elastic moduli may differ by orders of magnitude within soft tissues in various physiologic states (Sarvazyan *et al* 1995), (Skovoroda *et al* 1995b). In addition, manual self-examination is the first diagnostic line of defense against both breast (Hill *et al* 1988), (Newcomb *et al* 1991) and testicular cancers. With breast cancer, manual detection of a new mass often merits excisional biopsy, even if uncorroborated by other tests, as nodule hardness raises suspicion of malignancy (Foster 1996). Palpation of superficial lymph nodes and abdominal organs is also routinely performed. Although the touch of a skilled physician is a powerful diagnostic tool, palpation sensitivity is relatively poor within deep, dense or heterogeneous tissue. Thus, most manually detected lesions are either superficial, relatively large, or both.

### 1.2. Elasticity imaging

Currently, many scientists are working on extending the range and sensitivity of palpation by using various methods to image tissue elasticity. The basic method for creating an elasticity map involves two steps. First, the internal displacements within tissue under an applied mechanical stress are measured. The (usually externally) applied deformation may be either dynamic or static. Then, from these data, a reconstruction of regional variations in tissue elasticity is performed, either directly or after calculating internal strains. Although both internal displacements and strains are related to the elastic properties of tissue, both are strongly affected by geometry. Thus, some form of reconstruction is necessary to uniquely determine the elasticity distribution.

To date, two major medical imaging modalities have been used to measure tissue displacement: ultrasound and magnetic resonance imaging (MRI). The phase sensitivity of these methods lends itself to tracking tissue motion. Most elasticity imaging has been carried out using ultrasonically measured tissue displacements. These data have been obtained by tracking specular reflections (Dickinson and Hill 1982), (Tristram *et al* 1986, 1988), by Doppler techniques (Lerner *et al* 1990), (Parker *et al* 1990), (Parker and Lerner 1992), by cross-correlation of acoustic echoes (Ophir *et al* 1991), (Garra *et al* 1997), and by speckle tracking (Adler *et al* 1988), (O'Donnell *et al* 1994), (Emelianov *et al* 1995a). Other efforts employ MRI for measuring tissue motion, as discussed below.

### 1.3. MRI measurement of tissue displacement

In the past, myocardial motion and strain have been measured using spatial magnetization tagging (Axel and Dougherty 1988), (Zerhouni *et al* 1988), and phase-based velocity encoding (Pelc *et al* 1995). More recently, methods have been devised

to measure tissue displacement specifically for elasticity imaging. These measurements can be separated based upon the nature of the applied deformation.

*1.3.1. Dynamic deformation* With these methods, a periodic excitation is applied to the tissue near the region of interest, and the entire system may be allowed to reach steady state. One or several “snap shots” of mechanical wave propagation within the object are produced by controlling the relative phase between the mechanical excitation and the motion-encoding gradients. The local displacement information in these images is then used as an input for an elasticity reconstruction algorithm. Initial experiments used a shear excitation, and the elasticity reconstruction was performed assuming the recorded image contained only shear waves (Muthupillai *et al* 1995). If only shear waves are present in a purely elastic medium, local elastic modulus variations are determined via the relation  $\mu = \nu^2 \lambda^2 \rho$ , where  $\mu$  is the local shear modulus,  $\nu$  is the frequency of the applied deformation,  $\lambda$  is the measured local strain-wave wavelength, and  $\rho$  is the density of the medium. Although attractive in its simplicity, this approach is compromised by frequency dependent visco-elastic effects and strain-wave wavelength, interference from reflections off of elastic inhomogeneities, and the possible presence of longitudinal mechanical waves in the medium. Despite these limitations, this method has been applied *in vivo* (Dresner *et al* 1999), (Lawrence *et al* 1999). Recently, a more general elasticity reconstruction from a series of “instantaneous” steady state mechanical wave images has been developed (Sinkus *et al* 1999). This and another technique (Van Houten *et al* 1999), (Weaver *et al* 1999) rely on a more complete visco-elastic tissue model than that presented in Muthupillai *et al* (1995).

*1.3.2. Static deformation* Another method of producing an internal strain field in an object is to deform it and allow the material to relax to equilibrium before measuring the displacement field. The displacement field has been accessed using spatial magnetization tagging, but this method suffers from spatial resolution limited by the tagged grid size and typically measures only two-dimensional (2D) motion (Fowlkes *et al* 1995). A quasi-static method using bipolar gradient phase encoding of 2D motion is presented by Plewes *et al* (1995, 1996). Stimulated echo MRI has also been used to measure 2D displacement fields, from which elasticity images have been reconstructed (Chenevert *et al* 1998). This method has been extended to study myocardial motion (Aletras *et al* 1999). With these techniques, visco-elastic effects are generally ignored, making the reconstruction more straight-forward. Care must be taken, however, to justify the use of a static model, especially when repeated deformations are needed to acquire a complete data set.

In general, MRI has several advantages over ultrasound with respect to elasticity imaging. Although ultrasound accurately measures motion along the beam axis, lateral motion is measured with a resolution given by the depth-dependent beam width. Out-of-plane motion is generally not considered given the problems with three-dimensional (3D) image registration in ultrasound. These restrictions compromise the quality of

displacement data available and constrain the type of model used to produce an elasticity image. Ultrasound does, though, offer the advantages of low cost and real-time imaging. MRI, on the other hand, gives one the ability to measure 3D displacements within an object, and does this at a higher overall resolution than clinical ultrasound.

In this paper we present a method for encoding the full 3D displacement field within an object undergoing an externally applied static (or quasi-static) deformation. Local strain estimates are calculated from the measured displacements, and the strain tensor is used to numerically solve differential elasticity equilibrium equations, ultimately producing a 3D elasticity image.

## 2. Reconstructive elasticity imaging from static displacement fields

The goal of elasticity imaging is to produce a map of the tissue elastic modulus in a region of interest using available measurements of displacement components. In this work, the reconstruction approach taken is based upon a model of linear, elastic, isotropic media (Emelianov *et al* 1995b), (Skovoroda *et al* 1995a, 1999). The central equations and concepts are covered briefly here. A more detailed discussion can be found in the references mentioned.

### 2.1. Linear elasticity and reconstruction

In linear elasticity, the components of the strain ( $\epsilon_{ij}$ ) and stress ( $\sigma_{ij}$ ) tensors in an incompressible medium undergoing small deformations are given by:

$$\epsilon_{ij} = \frac{1}{2} \left( \frac{\partial u_i}{\partial x_j} + \frac{\partial u_j}{\partial x_i} \right) \quad (1)$$

$$\sigma_{ij} = p\delta_{ij} + 2\mu\epsilon_{ij} \quad (2)$$

where  $u_i$  is a component of the displacement vector  $\mathbf{U} = (u_1, u_2, u_3)$  in Cartesian coordinates  $\mathbf{r} = (x_1, x_2, x_3)$ ,  $p$  is the product  $\lambda \nabla \cdot \mathbf{U}$  for compressible media or the static internal pressure for incompressible media,  $\delta_{ij}$  is the Kronecker delta function,  $\lambda$  and  $\mu$  are the Lamé coefficients, and  $\mu = \mu(\mathbf{r})$  is the shear elastic modulus.

A medium undergoing static deformation obeys the equilibrium condition:

$$\sum_{j=1}^3 \frac{\partial \sigma_{ij}}{\partial x_j} + f_i = 0 \quad i = 1, 2, 3, \quad (3)$$

where  $f_i$  is the body force per unit volume acting in the  $x_i$  direction. In addition, if a medium is incompressible, volume conservation leads to the following relation:

$$\nabla \cdot \mathbf{U} = \epsilon_{11} + \epsilon_{22} + \epsilon_{33} = \frac{\partial u_1}{\partial x_1} + \frac{\partial u_2}{\partial x_2} + \frac{\partial u_3}{\partial x_3} = 0. \quad (4)$$

Although not necessary in the development that follows, it should be noted that soft tissue is approximately incompressible.

Using equations (1) and (2) in (3), the unknown  $p(\mathbf{r})$  can be eliminated to yield a set of differential equations depending only on  $\mathbf{U}$ , first and higher-order spatial derivatives



of  $U$ , and the elasticity distribution,  $\mu(\mathbf{r})$ . This set of equations is then numerically solved to estimate the unknown shear elasticity distribution.

## 2.2. Importance of three-dimensional reconstruction methods

Several approaches have been proposed to estimate tissue elasticity from the experimentally measured spatial distribution of internal displacements within an object. The simplest method is a one-dimensional (1D) estimation of normalized tissue elasticity, expressed as:

$$\kappa_1 = 1/\varepsilon, \quad (5)$$

where  $\varepsilon$  is longitudinal strain (Ophir *et al* 1991), (Garra *et al* 1997). Indeed, a loaded object generally exhibits low longitudinal strain in relatively hard regions and high longitudinal strain in relatively soft regions.

A 2D elasticity reconstruction, based on a plane-strain assumption and all necessary in-plane strain components, provides a more accurate representation of the object's elasticity (Skovoroda *et al* 1995a, 1999). The theory of reconstructing clearly bounded and spatially distributed tissue inhomogeneities has been demonstrated by Skovoroda *et al* (1995a) as well. However, inaccurate estimates may result by using either a 1D or 2D reconstruction of a 3D object.

To demonstrate these inaccuracies, consider a spherical inclusion of radius  $R$  in a uniaxially, uniformly loaded, infinite, homogeneous medium (Goudier 1933). For an incompressible medium, the distribution of longitudinal strain along the  $x_3$  axis (orthogonal to the applied deformation), is (Skovoroda *et al* 1994):

$$\varepsilon = \begin{cases} \frac{5\beta}{3+2\kappa_0} & x_3 \leq R \\ \beta \left\{ 1 + \frac{\kappa_0-1}{2(3+2\kappa_0)} \left[ 5 \left( \frac{R}{x_3} \right)^3 - 9 \left( \frac{R}{x_3} \right)^5 \right] \right\} & x_3 > R. \end{cases} \quad (6)$$

Here  $\beta$  is the magnitude of the applied strain and  $\kappa_0 = \mu/\mu_0$  is the ratio of the inclusion to background shear moduli.

Normalizing (6) by  $\beta$ , which corresponds to the axial strain in the tissue far from the inclusion, and substituting into (5) we obtain:

$$\kappa_1 = \begin{cases} \frac{3+2\kappa_0}{5} & x_3 \leq R \\ (3+2\kappa_0) \left\{ 3 + 2\kappa_0 + \frac{\kappa_0-1}{2} \left[ 5 \left( \frac{R}{x_3} \right)^3 - 9 \left( \frac{R}{x_3} \right)^5 \right] \right\} & x_3 > R. \end{cases} \quad (7)$$

Note that  $\kappa_1/\kappa_0 = (3+2\kappa_0)/5\kappa_0$  within the inclusion. That is, for a very hard inclusion ( $\kappa_0$  large), the relative modulus obtained from a 1D reconstruction will only be 40% of its actual value. On the other hand, for a soft inclusion ( $\kappa_0$  small), the relative modulus estimate will approach 3/5, *no matter how much softer the inclusion is than the background*. Obviously, the inaccuracy of a 1D elasticity estimation may not be acceptable for many applications.

Now consider a 2D reconstruction. Figures 1(a) and (e) show the exact relative elasticity distribution,  $\kappa(x_1, x_2)$ , for two infinitesimal planes in our pedagogic phantom

with  $\kappa_0 = 4$ . Figure 1(a) presents  $\kappa$  for  $x_3/R \approx 1.05$ , that is, outside of the inclusion, while figure 1(e) is the  $x_3/R \approx 0.95$  plane. The corresponding relative 2D reconstructions,  $\kappa_2(x_1, x_2)$ , are shown in figures 1(b) and (f). The reconstructions were performed using the algorithm presented by Skovoroda *et al* (1999). For comparison with experimental results (see section 5), an analytic model was used to generate displacement data which was sampled with the  $x_2$  resolution of the experimental displacement encoded data discussed in section 4.2. The strains used as input for the reconstructions were calculated as described in section 4.3, and the reconstructions were performed over a region of interest identical to the one discussed in that same section. The positions of the two reconstructed planes were selected to approximately correspond to the experimental planes presented in section 5. As evidenced here, neglecting out-of-plane strain components in the reconstruction results in geometrical distortions in the elasticity image. In this case, the spherical inclusion is reconstructed as a prolate spheroid. The reconstruction inaccuracy of a plane-strain based reconstruction is small near the central plane and increases with the distance between the imaging plane and the center of the inclusion. Far from the inclusion, a 2D reconstruction would again be accurate.

It is clear that a 1D or 2D reconstruction may lead to significant inaccuracies in tissue elasticity estimations, especially when complicated *in vivo* geometries influence displacement and strain measurements. This points to the need for an accurate 3D elasticity reconstruction. As shown in (Skovoroda *et al* 1995a, 1999), a general unknown shear elasticity distribution,  $\mu(x_1, x_2, x_3)$ , must satisfy the equation:

$$\frac{\partial^2(\mu\epsilon_{12})}{\partial x_1^2} - \frac{\partial^2(\mu\epsilon_{12})}{\partial x_2^2} + \frac{\partial^2[\mu(\epsilon_{22} - \epsilon_{11})]}{\partial x_1 \partial x_2} + \frac{\partial^2(\mu\epsilon_{23})}{\partial x_1 \partial x_3} + \frac{\partial^2(\mu\epsilon_{13})}{\partial x_2 \partial x_3} = 0. \quad (8)$$

Thus, in order to compute all the necessary components of the strain tensor,  $\epsilon_{ij}$ , in (8), all of the displacement components ( $u_1, u_2, u_3$ ) must be measured as a function of spatial coordinates ( $x_1, x_2, x_3$ ). This requirement exists in both the differential-based 3D reconstruction (8), as well as in the more stable integral based 3D approach (Skovoroda *et al* 1999).

The 3D elasticity reconstructions from the two planes previously discussed are shown in figures 1(c) and (g). The reconstruction was performed as discussed in section 4.3. Although not perfect due to the relatively large  $x_3$  step size, the 3D reconstructions clearly exhibit fewer geometric distortions than the 2D estimates. This is particularly well illustrated by the central vertical profiles through the analytic, 2D, and 3D shear distributions presented in figures 1(d) and (h). In the  $x_3/R \approx 1.05$  plane, the 2D reconstruction estimates that an inclusion is present, when indeed it is not, while the 3D reconstruction shows little evidence of the presence of an inclusion. The estimate of the extent of the inclusion in the  $x_3/R \approx 0.95$  plane is also improved over the 2D estimate. As with the 2D reconstructions, the strain data and reconstruction parameters used for the 3D reconstruction were identical to those of the experimental parameters described in sections 4.2, 4.3, and 5.

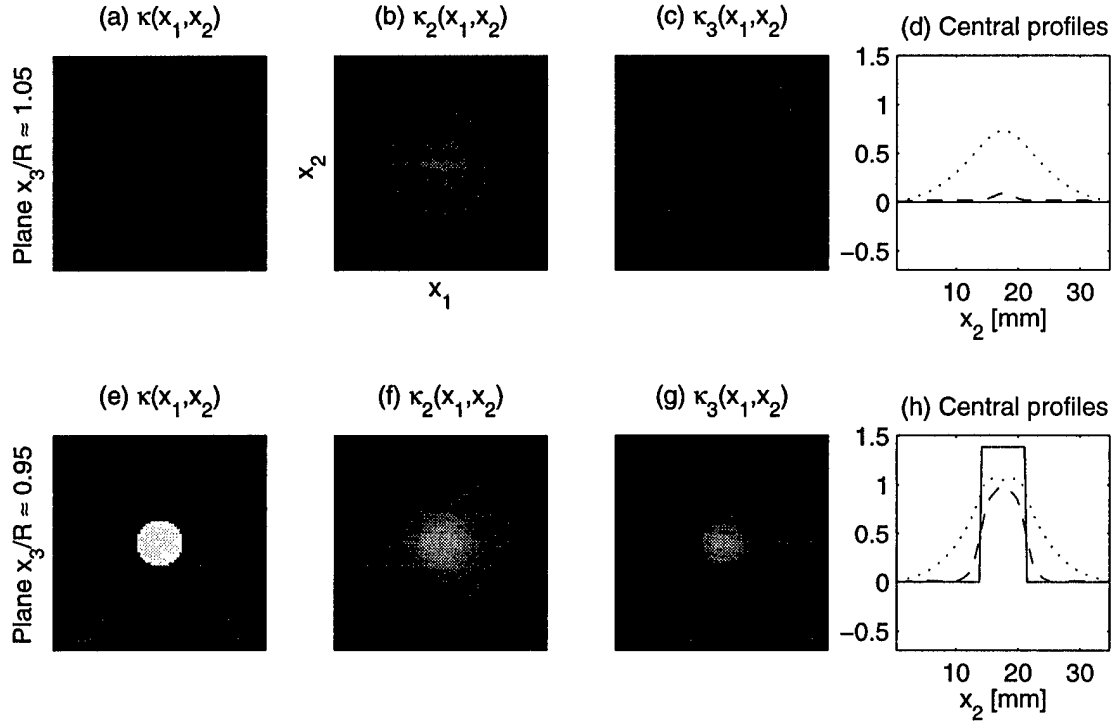


**Figure 1.** Simulated elasticity distributions,  $\kappa(x_1, x_2)$ , and corresponding 2D,  $\kappa_2(x_1, x_2)$ , and 3D,  $\kappa_3(x_1, x_2)$  elasticity reconstructions from the  $x_3/R \approx 1.05$ , (a)–(d), and  $x_3/R \approx 0.95$ , (e)–(h), planes of a phantom with a single hard, spherical inclusion of radius  $R$ . Also presented are the central vertical profiles of each distribution, where (—) is  $\kappa$ , (.....) is  $\kappa_2$ , and (---) is  $\kappa_3$ . All are presented on a log scale where black corresponds to a relative shear modulus of 0.5 and white to 4.5. The background has a relative shear modulus of 1, and the inclusion, 4.

### 3. Static displacement measurement via stimulated echo MRI

As previously discussed, static displacement measurements for elasticity imaging avoid several confounding factors that may be present if dynamic displacement measurements are used. Since shear wave propagation speed in soft tissue is approximately  $1\text{--}20\text{ m s}^{-1}$ , shear waves launched into a medium by an applied deformation may require tens of milliseconds to traverse an object approximately 100 mm in size. Reflected waves may take much longer to dampen. To appropriately measure an object's internal static displacements, the object must be in mechanical equilibrium—that is, it must satisfy (3)—during both the pre- and post-deformation measurements. A stimulated echo MRI sequence using displacement encoding gradient pulses is employed to achieve this (Chenevert *et al* 1998). Figure 2 presents a schematic of this pulse sequence. The mechanical transition from the pre- to post-deformational states occurs during the stimulated echo mixing time,  $T_M$ . Because the relevant magnetization is longitudinal during  $T_M$ , it is unaffected by the object's motion during the mechanical transition

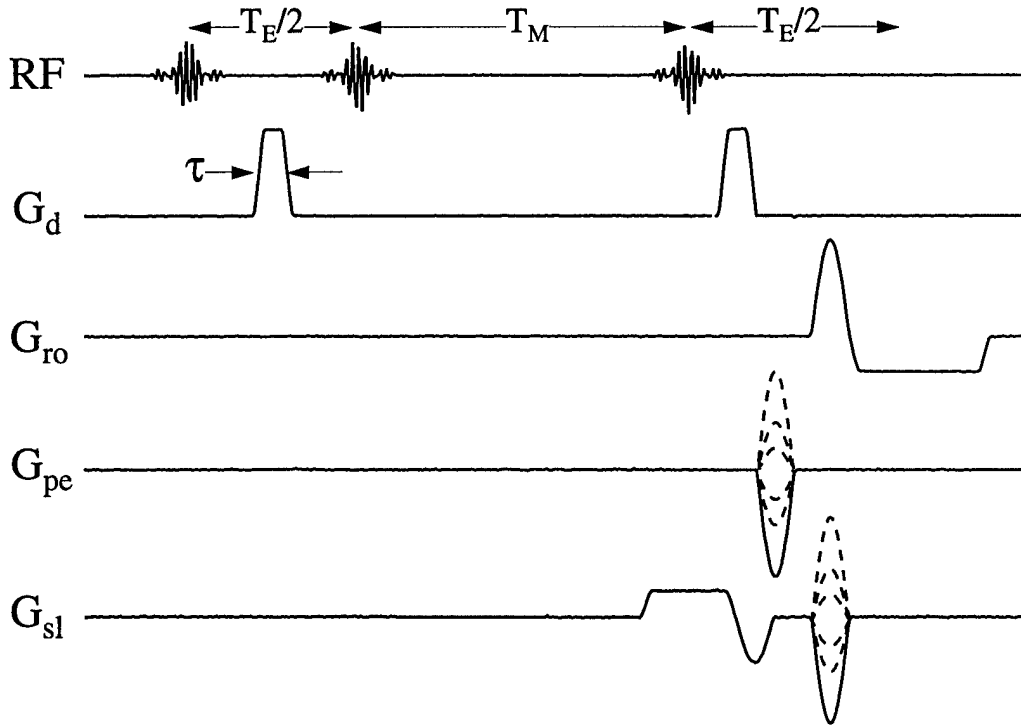


**Figure 2.** Displacement encoding, stimulated echo pulse sequence waveforms. RF = radio frequency,  $G_d$  = displacement encoding gradient, and  $G_{ro}$  = read-out ( $x_1$ ),  $G_{pe}$  = phase-encode ( $x_2$ ), and  $G_{sl}$  = slice ( $x_3$ ) directed gradient waveforms.  $T_M$  is the mixing time,  $T_E$  is the echo time, and  $\tau$  is the duration of the displacement encoding gradient. Note that the displacement encoding gradient may be applied to any of the directional waveforms.

period. This allows a more accurate measurement of static internal displacement. Additionally, precise synchronization of the motion and applied gradients is not necessary as long as the mechanical deformation begins after the second radio-frequency pulse, and internal motion stops before the third. A long delay in the echo time,  $T_E$ , could also be used to let the object reach equilibrium, but this would likely lead to prohibitive signal loss from  $T_2$  decay.

Local displacements are encoded in the magnetization's phase via pulsed-field gradients. The displacement sensitivity, in radians/distance, of the sequence is:

$$\Phi_d = \gamma \int_0^\tau G_d(t) dt = \gamma G_d \tau, \quad (9)$$

where  $\gamma$  is the gyromagnetic ratio of the proton,  $G_d(t)$  is the encoding gradient waveform, and  $\tau$  is the duration of the encoding gradient. However, for accurate displacement measurements, phase shifts unrelated to the applied deformation must

be removed. This is done by acquiring a phase reference data set using the same pulse sequence, but with the object maintained in the post-deformational state for the entire experiment. Note that all spatial encoding takes place with the object in the post-deformational state for both the displacement encoded and reference acquisitions. Thus, no image registration or tracking algorithms are required to use the reference data,  $S_r$ , to correct the displacement encoded data,  $S_d$ . The corrected data set,  $S_c$ , is then:

$$S_c(\mathbf{r}) = \frac{S_d(\mathbf{r})S_r(\mathbf{r})^*}{|S_r(\mathbf{r})|} \approx |S_d(\mathbf{r})|e^{i\phi(\mathbf{r})}. \quad (10)$$

Most sources of phase error, such as static field inhomogeneities, tend to be slowly varying functions of position. Thus the phase reference data may be acquired at relatively low spatial resolution to reduce scan time.

The unwrapped phase of (10) is related to the local displacement vector,  $\mathbf{U}$ , via:

$$\phi(\mathbf{r}) = \Phi_d \cdot \Delta \mathbf{r} = \Phi_d \cdot \mathbf{U}(\mathbf{r}), \quad (11)$$

where  $\Delta \mathbf{r}$  is the local displacement from pre- to post-deformational states. The displacement sensitivity,  $\Phi_d$ , may be made sensitive to motion in an arbitrary direction based upon appropriate combination of displacement encoding gradients in the read-out, phase-encode, and slice directions. Hence, this pulse sequence readily extends to acquiring three-dimensional displacement data.

## 4. Methods

### 4.1. Phantom

Elasticity imaging experiments were performed on a phantom with a spherical hard inclusion. Semicosil 921 silicone gel (Wacker Silicones Corporation, Adrian, MI) was used to construct a phantom qualitatively simulating the mechanical properties of soft tissue. The Semicosil 921 consists of two components, A and B, wherein different ratios of these components are used to vary the mechanical properties of the gel. A tissue-mimicking phantom was constructed in several steps. First, background material was prepared by thoroughly mixing components A and B in a 1:1 ratio, and then pouring the mixture into a 154-mm by 80-mm rectangular mold. The mixture was degassed and cured for 24 hours at room temperature to produce a 22-mm thick layer. Then a 25-mm diameter hard sphere was prepared from a 1:2.5 mixture of A and B and was placed on top of the layer in the middle of the mold. Finally, another batch of background material (1:1 ratio) was poured into the mold resulting in a 64-mm by 80-mm by 154-mm phantom with a single, hard, spherical inclusion roughly in the center. At the same time, three samples of each batch were taken to independently assess the elasticity contrast between the inclusion and surrounding materials. These measurements were performed using the force-deformation system described in (Erkamp *et al* 1998), and showed that the inclusion was four times harder than the background, and that both background materials were elastically equivalent.

#### 4.2. Data acquisition

To provide repeatable deformation, the phantom was placed under moderate pre-load pressure between two acrylic plates in a pneumatically driven device. Air-filled neoprene boots in a push-push configuration provided the necessary force to the top plate to keep the phantom in this pre-load state, and aided the vertical recoil of the phantom to the post-deformation state. Pneumatic pressure was delivered via two solenoid valves whose timing was controlled by an external transistor-transistor logic circuit triggered by the pulse sequence. Quick-release valves aided in depressurizing the boots. Both the pre-load and recoil positions of the top acrylic plate were set by adjustable stops; the bottom plate's position was fixed. The applied vertical deformation was approximately 2.4 mm, or about 6% strain, between the pre-transition (greater deformation) and post-transition (less deformation) states.

During data acquisition, the displacement encoding gradient pulse duration,  $\tau$ , was 1.5 ms, and the amplitude,  $G_d$ , was 40 mT m<sup>-1</sup> in the read-out ( $x_1$ ) and phase-encode ( $x_2$ ) directions, and 60 mT m<sup>-1</sup> in the slice ( $x_3$ ) direction. Here, the  $x_3$  direction was along the bore's axis, and the  $x_1$  and  $x_2$  directions were perpendicular to  $x_3$  in the horizontal and vertical directions, respectively. By (9), the displacement sensitivity,  $\Phi_d$ , was approximately 5.11  $\pi$  mm<sup>-1</sup> in the  $x_1$  and  $x_2$  directions, and about 7.66  $\pi$  mm<sup>-1</sup> in the  $x_3$  direction. The displacement encoding direction was cycled each pulse repetition between the  $x_1$ ,  $x_2$ , and  $x_3$  directions. The pulse-to-pulse repetition time was approximately 0.98 s, the mixing time ( $T_M$ ) was 270 ms, and the echo time ( $T_E$ ) was 45 ms. Two averages were taken of a 256  $\times$  256  $\times$  32 matrix covering an 80-mm by 110-mm by 48-mm field of view. The phase reference data were collected using a 256  $\times$  32  $\times$  32 matrix while keeping all other parameters the same. All experiments were performed on a 2 T, 18-cm bore MRI system (Bruker, formerly GE NMR Instruments) using a 150-mm transmit/receive birdcage coil.

#### 4.3. Data processing

All time-domain data were transferred off-line for processing. For phase correction, the phase reference data set was zero-filled to a 256  $\times$  256  $\times$  32 matrix. Then this and the displacement encoded data were 3D Fourier transformed and corrected as in (10). The resulting phase maps were then used to estimate the spatial derivatives to compute the strains, via (1), necessary for the elasticity reconstruction. Phase unwrapping of the displacement data was not required since only phase derivatives were used in the strain calculations. The displacement derivative at the  $i$ th point in the  $j$  direction was computed from the angle of the complex multiplication of the  $i + 1$ th point with the conjugate of the  $i - 1$ th point, then scaling by  $1/2\Phi_d^j$ , where  $\Phi_d^j$  is the magnitude of the displacement sensitivity in the  $j$  direction. For convenience, the strain data were decimated to the  $x_2$  step size in each  $x_3$  plane in order to have equal resolution in both the  $x_1$  and  $x_2$  directions. The strain images were then median filtered with a 5  $\times$  5 window, resulting in a slight decrease in spatial resolution. These strains were used as

input for the elasticity reconstruction.

The 3D elasticity reconstruction was performed using the least-squared error minimization algorithm discussed in Skovoroda *et al* (1999), with a second-order, one-sided finite derivative approximation in the  $x_3$  direction. The reconstruction of  $\mu(\mathbf{r})$  is a boundary value problem, therefore a unique solution is obtained only with boundary conditions. So a square 35-mm by 35-mm region of interest, which contained the inclusion in several  $x_3$  planes, was identified in the  $x_1$  and  $x_2$  directions. Along the boundaries of these regions, and in the first two  $x_3$  planes furthest from the center of the inclusion, the value of the shear modulus was set to one, resulting in a relative shear modulus reconstruction.

## 5. Results

Representative magnitude and corrected phase images of the Semicosil phantom for a 1.5-mm thick plane centered about  $x_3 = 0.75$  mm, or  $x_3/R \approx 0.05$ , are shown in figure 3. Knowing that  $\Phi_d \approx 5.11 \pi \text{ mm}^{-1}$  in the  $x_1$  and  $x_2$  directions, the number of  $2\pi$  phase wraps in figure 3(c) indicates a vertical deformation of approximately 2.3 mm, and those in figure 3(b) a horizontal deformation of about 2.0 mm. Reduced phase slope in the region of the hard inclusion is clearly visible in these figures as well. Due to the central location of this plane, there is little feature in  $\phi_3$  (part (d)).

Figure 4 shows representative strain maps from the planes centered around  $x_3 = 15.75$  mm and  $x_3 = 14.25$  mm. Due to the loaded state of the phantom during imaging, the sphere became prolate, therefore these planes correspond to the  $x_3/R \approx 1.05$  and  $x_3/R \approx 0.95$  locations, respectively. One normal strain,  $\varepsilon_{22}$  (parts (a) and (e)), the in-plane shear strain,  $\varepsilon_{12} = \varepsilon_{21}$  (parts (b) and (f)), and one through-plane shear strain,  $\varepsilon_{13} = \varepsilon_{31}$  (parts (c) and (g)), are shown for each plane. These components are all required to perform the elasticity reconstruction in (8). Note that the presence of through-plane strains in (8) necessitates measurement of the full 3D displacement field. In addition, although elasticity specific details are seen in the strain maps, features related to geometry and the applied deformation are also clearly present. This points to the need for a proper elasticity reconstruction in order to obviate these confounding factors. Also shown are the traces of the strain tensor,  $\varepsilon_{11} + \varepsilon_{22} + \varepsilon_{33}$ , for both planes (parts (d) and (h)). The relative lack of features in the trace of the strain tensor indicates that the phantom is nearly incompressible (like soft tissue).

Magnitude images of the 35-mm by 35-mm regions of interest in the same two planes, along with two different shear modulus reconstructions of these planes, are presented in figure 5. As clearly seen in the magnitude images, the hard inclusion is present in the  $x_3/R \approx 0.95$  plane, while it is absent in the  $x_3/R \approx 1.05$  plane. Figures 5(b) and (f) show 2D elasticity reconstructions of these two planes, while figures 5(c) and (g) show the corresponding 3D elasticity reconstructions. As in figure 1, one sees an over-estimate of the 3D spatial extent of the inclusion in the 2D reconstructions. This over-estimate is corrected with the 3D reconstruction. For ease of comparison,

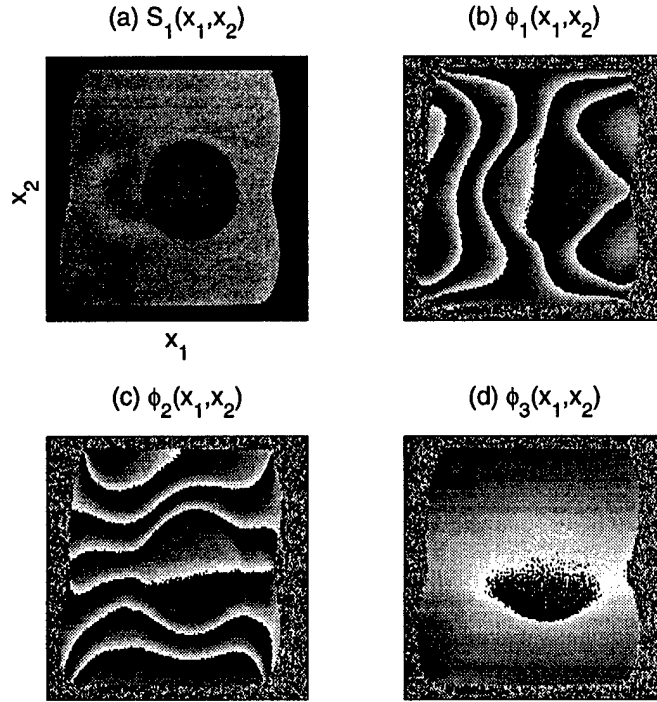


**Figure 3.** Representative magnitude and phase images from the  $x_3/R \approx 0.05$  plane of the 3D displacement encoded data set from a phantom with a single, hard, spherical inclusion.  $S_1$ , (a), is the magnitude of the  $x_1$ -displacement encoded data, and  $\phi_i$ , (b)–(d), are the phase images of the  $x_i$ -displacement encoded data.

vertical profiles through the center of the inclusion from the magnitude, 2D, and 3D reconstructions are presented in figures 5(d) and (h). Note that the magnitude images only convey geometric information.

## 6. Discussion

The stimulated echo sequence presented phase encodes internal displacements using gradient pulses. An externally applied deformation, synchronized with the pulse sequence, produces an internal displacement field. This deformation is actively driven with a pneumatic device, and the mechanical transition from pre- to post-deformation occurs during the sequence mixing time,  $T_M$ , while the relevant magnetization is longitudinal. Because longitudinal magnetization decays only as  $T_1$ , the mechanical transition period may be extended to allow potentially long-lived or ill-defined motions within the object to dampen. With a sufficiently long  $T_M$ , the encoded displacement will be approximately static. However, signal loss due to  $T_1$  relaxation sets a practical limit on the length of  $T_M$ . To determine an appropriate mixing time, a series of 2D displacement encoded images was taken, varying  $T_M$  from 50–750 ms. From the phase maps of these data, one could see that the top acrylic plate of the deformation device



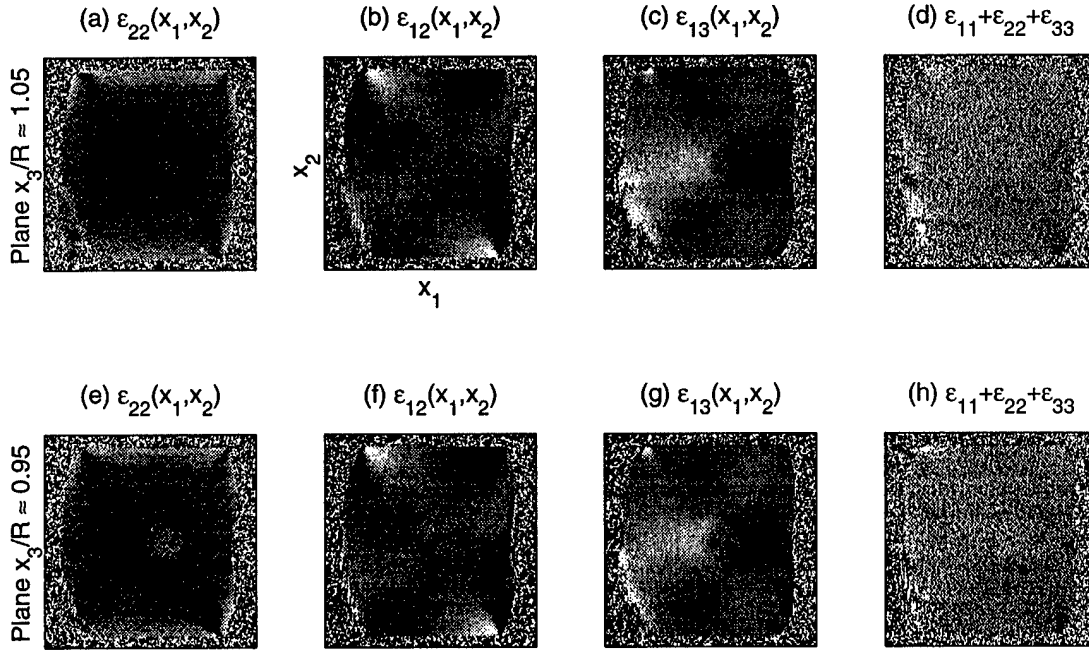


**Figure 4.** Representative strain images from the  $x_3/R \approx 1.05$ , (a)–(d), and  $x_3/R \approx 0.95$ , (e)–(h), planes from the 3D displacement encoded data of the phantom with a single, hard, spherical inclusion. One longitudinal strain,  $\varepsilon_{22}$ , the in-plane shear strain,  $\varepsilon_{12} = \varepsilon_{21}$ , one through-plane shear strain,  $\varepsilon_{13} = \varepsilon_{31}$ , and the trace of the strain tensor,  $\varepsilon_{11} + \varepsilon_{22} + \varepsilon_{33}$ , are presented for each plane. Linear scales for each image are, from black to white: (a), (e):  $[-0.08, 0.03]$ ; (b), (f):  $[-0.05, 0.05]$ ; (c), (d), (g), (h):  $[-0.03, 0.03]$ .

completed its excursion in under 200 ms, and the internal motion in the phantom became negligible by 250 ms. To ensure that (3) was reasonably satisfied, a 270 ms mixing time was chosen for subsequent data collection. Although the deformation device used here provides adequate transition speed, an even faster device would allow a shorter  $T_M$ , yielding more signal. While absent in the phantom used here, water diffusion in the presence of displacement encoding gradients will be another source of signal loss in *in vivo* experiments. This loss can be mitigated by reducing the displacement sensitivity,  $\Phi_d$ , or by shortening  $T_M$ .

The quality of the shear modulus reconstruction ultimately depends on the local phase, as in (11), induced by the encoding gradients and the local displacement. More specifically, the quality depends on the spatial derivatives of the encoded phase. A study of the effects of displacement sensitivity, applied deformation, relative hardness, and diffusion loss on the signal-to-noise ratio (SNR) of the elasticity reconstruction has been presented in (Steele *et al* 1999). This study demonstrates that increased intra-voxel phase wrap will increase the reconstruction SNR, up to a  $\pi$  intra-voxel phase distribution. Note that the reconstruction SNR increases despite a reduction in the nuclear magnetic resonance (NMR) signal from the object. Assuming a linear

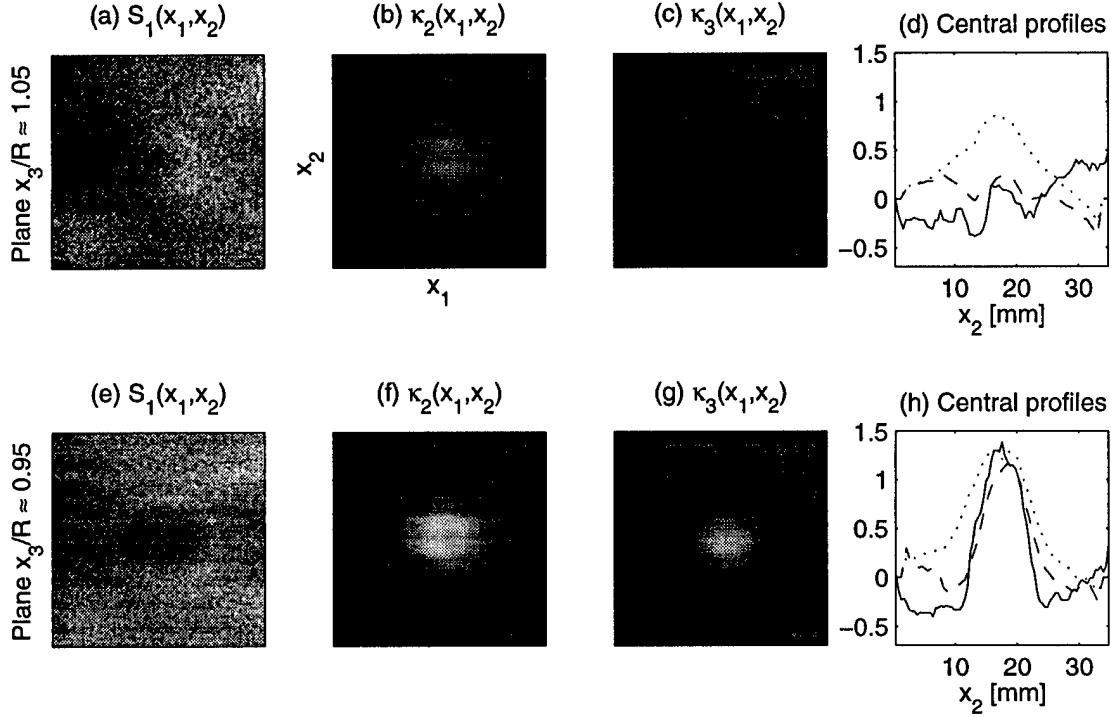


**Figure 5.**  $x_1$ -displacement encoded magnitude images,  $S_1(x_1, x_2)$ , and corresponding 2D,  $\kappa_2(x_1, x_2)$ , and 3D,  $\kappa_3(x_1, x_2)$  elasticity reconstructions from the  $x_3/R \approx 1.05$ , (a)–(d), and  $x_3/R \approx 0.95$ , (e)–(h), planes of a phantom with a single hard, spherical inclusion. Also presented are the central vertical profiles of each distribution, where ( $\cdots$ ) is  $\kappa_2$ , and ( $---$ ) is  $\kappa_3$ . All are presented on a log scale where black corresponds to a relative shear modulus of 0.5 and white to 4.5. The background has a relative shear modulus of 1, and the inclusion, 4, from independent measurements. For geometric reference purposes, parts (d) and (h) include plots of  $S_1^{-1}$  (filtered and normalized) as ( $---$ ).

phase distribution of  $\theta$  radians across a voxel, the signal modulation from that voxel will be  $|\text{sinc}(\theta/2)| = |\sin(\theta/2)(\theta/2)^{-1}|$ . However, the phase gradients (that is, the displacement derivatives) will be maximized without aliasing as the intra-voxel phase wrap approaches  $\pi$ , and this is the signal that is important in the reconstruction. A  $\pi$  phase wrap may be achieved through many combinations of applied deformation and displacement sensitivity. However, increasing  $\Phi_d$  will increase signal loss due to diffusion, as discussed above. Hence, a smaller displacement sensitivity and increased deformation would appear to be optimal. Again, there is a trade-off: as deformation increases, the model of linear elasticity discussed in section 2.1 will become less and less valid. Elasticity reconstructions from finite displacement fields have been demonstrated in Skovoroda *et al* (1999), but these are obviously more computationally intensive than the linear reconstructions used here. In relation to the data presented here, the number of  $2\pi$  phase bands across the phantom in figure 3 clearly indicate that this data was

acquired with a sub-optimal displacement sensitivity/applied deformation combination. Because neither the encoding nor the deformation used here were extreme, the elasticity reconstruction's SNR should be relatively easily improved merely by optimizing the intra-voxel phase wrap.

Relative hardness, object geometry, and deformation geometry also effect the displacement phase gradients. In general, the phase gradients increase near soft/hard interfaces and are higher in relatively soft regions of tissue. Excessive phase wrap (i.e. strain) can lead to regions of significant signal loss in a manner analogous to flow dephasing in conventional MRI. The resulting reconstructions would suffer from this signal loss. Hence, the applied deformation and displacement sensitivity should be optimized for the regions of highest strain in an object. Increased intra-voxel phase wrap in regions of lower strain may be obtained by integrating the signal from several voxels; in essence, applying an adaptive voxel size based upon local phase gradients. This increase in signal would come at the expense of spatial resolution. Additionally, signal loss in the displacement encoded magnitude images may be useful for identifying high strain regions in tissue.

Another factor affecting the displacement signal is the reproducibility of the applied deformation. For multi-step acquisitions, as those presented here, good deformation reproducibility is essential. Variations in the applied deformation will lead to phase instability, motion-like artifacts, and errors that will propagate through the elasticity reconstruction. Adequate reproducibility has been achieved with the current deformation system. However, irreproducible or asynchronous motions within the imaged object may be problematic. These would include physiologic cardiac and respiratory motion present in *in vivo* experiments. In some ways, the problems associated with undesired motion would be similar to those encountered in diffusion MRI. Because the applied deformation is external, though, the displacement encoding can be tailored to it, reducing the effect of undesired motion on the displacement data. Additional complications arise because phase derivatives of the displacement data, approximated by finite differences, are required for reconstruction. In addition to choosing an appropriate deformation/encoding combination, methods should be devised to reduce the effects of undesired motion on the displacement derivatives.

Clearly several advantages justify performing a 3D elasticity reconstruction rather than a 2D reconstruction. As illustrated in figures 1 and 5, and as discussed in sections 2.2 and 5, a 3D reconstruction provides a more accurate representation of the elasticity distribution than a 2D reconstruction in the simple phantom used here. Complicated *in vivo* geometries will only increase the likelihood that neglecting out-of-plane strain components will result in an inaccurate elasticity estimate. This increased accuracy comes, though, at the expense of increased computational complexity and increased scan time. This increase in scan time may be lessened through the use of echo-planar imaging (Mansfield and Pykett 1978) or fast spin-echoes (Hennig *et al* 1986) for spatial encoding (Chenevert *et al* 1999). It should also be noted that the reconstruction in (8) does not rely on the assumption of incompressibility, although making this assumption

provides another means of regularizing the reconstruction.

Additionally, a reconstruction of static displacement data offers several advantages over a reconstruction of dynamic displacement data. A static reconstruction allows one to ignore visco-elastic effects as well as the longitudinal or shear nature of the applied deformation. Static methods also provide high SNR displacement and strain estimates. Dynamic methods, on the other hand, provide a potentially very simple reconstruction (Muthupillai *et al* 1995). However, as previously noted in section 1.3.1, this reconstruction may be compromised by interference from elastic inhomogeneities, attenuation of shear waves, mixing of longitudinal and shear waves, and resolution limits imposed by the shear-wave wavelength. Reconstruction models that include visco-elastic effects allow a more accurate interpretation of dynamic data (Sinkus *et al* 1999), (Van Houten *et al* 1999), but these are necessarily more complicated than static models (Skovoroda *et al* 1995a, 1999).

Choosing a contour of constant shear modulus for appropriate boundary conditions for (8), though, can, in practice, be a challenge. In the applications discussed here, *a priori* knowledge of phantom geometry was employed in the reconstructions. This may be possible *in vivo* as well, albeit more complicated. For instance, in breast elasticity imaging, such a contour may be defined in the subcutaneous fat surrounding the parenchyma using the boundary detection procedure described in Skovoroda *et al* (1995a). The elasticity reconstruction would then be relative to the shear modulus of the fat boundary, assuming that it is constant. Alternatively, a high signal cuff of known elastic modulus could be used to surround the breast. This would provide an absolute image of shear modulus variations if the boundary contour were chosen inside the cuff.

The 3D shear elasticity reconstructions presented above contain artifacts both inside and outside of the inclusion due to the finite SNR in the measured displacement strain components, and due to the step size used in the finite approximation to the derivatives in (8). In contrast to the 2D elasticity reconstruction, where the elasticity distribution is reconstructed independently in each plane, the 3D reconstruction uses the elasticity distribution in neighboring planes. Therefore, in addition to in-plane error propagation problems discussed elsewhere (Skovoroda *et al* 1995a), error propagation in the through-plane direction may occur due to inaccurate elasticity reconstructions in the preceding planes. This is particularly true if the 3D elasticity reconstruction is performed, as in this paper, by solving an initial value problem in the through-plane direction. Even though the more stable integral based approach (Skovoroda *et al* 1999) was employed to solve (8) for each plane, the results of the 3D elasticity reconstructions in subsequent planes exhibit significant error propagation in the  $x_3$  direction.

Given a particular spatial discretization of the displacement data, the error propagation can be reduced by several approaches. These include more appropriate data filtering and choice of boundary conditions, but these considerations are beyond the scope of this paper.

These include more appropriate data filtering and development of less sensitive to noise elasticity reconstruction, but these considerations are beyond the scope of this

paper.

## 7. Conclusions

The ultimate goal of quantitative elasticity imaging is to provide physicians with a method of remotely palpating soft tissue to detect disease. The three dimensional elasticity imaging technique demonstrated here is a step toward extending the range and sensitivity of palpation, a powerful diagnostic tool. One possible application of this technique would be measuring the elasticity of breast tissue normally inaccessible to manual palpation. A large elastic modulus difference between normal and pathological breast tissue has been measured *in situ*. A previously mentioned study indicates that soft tissues in different physiologic states display shear modulus variations of 1–2 orders of magnitude (Sarvazyan *et al* 1995). If these elastic changes predate calcification formation, elasticity imaging may increase sensitivity to and characterization of malignant breast masses, complementing existing diagnostic tools. The relatively high cost of MRI may hinder using this approach as a general screening technique. However, additional work to define the role of this modality as a primary or complementary diagnostic tool in diseases of soft tissues seems worthwhile indeed.

## Acknowledgments

The authors would like to thank M. O'Donnell for helpful discussions and suggestions, and R. Erkamp for the direct mechanical measurements of samples. This research was funded in part by the National Institutes of Health grant DK47324 and by US Army grant DAMD17-97-7079.

## References

- Adler R, Rubin J M, Bland P and Carson P 1988 *Med. Phys.* **16** 333–7
- Aletras A H, Ding S J, Balaban R S and Wen H, *J. Magn. Reson.* **137** 247–52
- Axel L and Dougherty L 1988 *Radiology* **169** 59–63
- Chenevert T L, Skovoroda A R, O'Donnell M and Emelianov S Y 1998 *Magn. Reson. Med.* **39** 482–90
- Chenevert T L, Steele D D, Emelianov S Y and O'Donnell M 1999 *Proc. ISMRM, 7th Scientific Meeting and Exhibition (Philadelphia)* p 263
- Dickinson R J and Hill C R 1982 *Ultrasound Med. Biol.* **8** 263–71
- Dresner M A, Rossman P J, Kruse S A and Ehman R L 1999 *Proc. ISMRM, 7th Scientific Meeting and Exhibition (Philadelphia)* p 526
- Emelianov S Y, Lubinski M A, Weitzel W F, Wiggins R C, Skovoroda A R and O'Donnell M 1995a *Ultrasound Med. Biol.* **21** 871–83
- Emelianov S Y, Skovoroda A R, Lubinski M A and O'Donnell M 1995b *Acoustical Imaging* vol 21 (New York: Plenum Press) pp 241–53
- Erkamp R Q, Wiggins P, Skovoroda A R, Emelianov S Y and O'Donnell M 1998 *Ultrason. Imaging* **20** 17–28
- Foster R S Jr 1996 *Diseases of the Breast* ed J R Harris *et al* (Philadelphia: Lippincott-Raven) 133–8
- Fowlkes J B, Emelianov S Y, Pipe J G, Skovoroda A R, Adler R S and Carson P L 1995 *Med. Phys.* **22** 1771–8

- Garra B S, Cespedes E I, Ophir J, Spratt S R, Zuurbier R A, Magnant C M and Pennanen M F 1997 *Radiology* **202** 79-86
- Goudier J 1933 *Trans. ASME* **55** 39-44
- Hennig J, Nauerth A and Friedburg H 1986 *Magn. Reson. Med.* **3** 823-33
- Hill D, White V, Jolley D and Mapperson K 1988 *Br. J. Med.* **297** 271-5
- Lawrence A J, Rossman P J, Mahowald J L, Manduca A, Hartmann L C and Ehman R L 1999 *Proc. ISMRM, 7th Scientific Meeting and Exhibition (Philadelphia)* p 525
- Lerner R M, Huang S R and Parker K J 1990 *Ultrasound Med. Biol.* **16** 231-9
- Mansfield P and Pykett I L 1978 *J. Magn. Reson.* **29** 355
- Muthupillai R, Lomas D J, Rossman P J, Greenleaf J F, Manduca A and Ehman R L *Science* **269** 1854-7
- Newcomb P A, Weiss S, Storer B E, Scholes D and Young B E *J. Natl. Cancer Inst.* **83** 260-5
- O'Donnell M, Skovoroda A R, Shapo B M and Emelianov S Y 1994 *IEEE Trans. Ultrason. Ferroelectrics and Frequency Control* **42** 314-25
- Ophir J, Cespedes E I, Ponnekanti H, Yazdi Y and Li X 1991 *Ultrason. Imaging* **13** 111-34
- Parker K J, Huang S R, Musulin R A and Lerner R M 1990 *Ultrasound Med. Biol.* **16** 241-6
- Parker K J and Lerner R M 1992 *J. Ultrasound Med.* **11** 387-92
- Pelc N J, Drangova M, Pelc L R, Zhu Y, Noll D C, Bowman B S and Herfkens R J 1995 *J. Magn. Reson. Imaging* **5** 339-45
- Plewes D B, Betty I, Urchuk S N and Soutar I 1995 *J. Magn. Reson. Imaging* **5** 733-8
- Plewes D B, Poole G, Leitch M and Urchuk S N 1996 *Proc. ISMRM, 4th Scientific Meeting and Exhibition (New York)* p 476
- Sarvazyan A P, Skovoroda A R, Emelianov S Y, Fowlkes J B, Pipe, J G, Adler R S, Buxton R B and Carson P L 1995 *Acoustical Imaging* vol 21 (New York: Plenum Press) pp 223-40
- Sinkus R, Lorenzen J, Schrader D, Lorenzen M, Dargatz M and Holz D 1999 *Proc. ISMRM, 7th Scientific Meeting and Exhibition (Philadelphia)* p 259
- Skovoroda A R, Emelianov S Y and O'Donnell M 1995a *IEEE Trans. Ultrason. Ferroelectrics and Frequency Control* **41** 302-13
- Skovoroda A R, Emelianov S Y, Lubinski M A, Sarvazyan A P and O'Donnell M 1994 *IEEE Trans. Ultrason. Ferroelectrics and Frequency Control* **41** 302-13
- Skovoroda A R, Klishko A N, Gukasyan D A, Maevsky E I, Ermilova V D, Oranskaya G A and Sarvazyan A P 1995b *Biofizika* **40** 1335-40
- Skovoroda A R, Lubinski M A, Emelianov S Y and O'Donnell M 1999 *IEEE Trans. Ultrason. Ferroelectrics and Frequency Control* **46** 523-35
- Steele D D, Chenevert T L, Emelianov S Y and O'Donnell M 1999 *Proc. ISMRM, 7th Scientific Meeting and Exhibition (Philadelphia)* p 1616
- Tristram M, Barbosa D C, Cosgrove D O, Nassiri D K, Bamber J C and Hill C R 1986 *Ultrasound Med. Biol.* **12** 927-37
- Tristram M, Barbosa D C, Cosgrove D O, Bamber J C and Hill C R 1988 *Ultrasound Med. Biol.* **14** 695-707
- Van Houten E, Miga M I, Kennedy F E, Weaver J B and Paulsen K D 1999 *Proc. ISMRM, 7th Scientific Meeting and Exhibition (Philadelphia)* p 260
- Weaver J B, Van Houten E, Miga M I, Kennedy F E, Hartov A, Poplack S P, Nagy H M and Paulsen K D 1999 *Proc. ISMRM, 7th Scientific Meeting and Exhibition (Philadelphia)* p 1617
- Zerhouni E A, Parish D M, Rogers W J, Yang A and Shapiro E P 1988 *Radiology* **169** 164-72

## INTRODUCTION

Elasticity imaging may offer clinicians a non-invasive method of remotely palpating patients to detect diseased tissues. Tissue elasticity information may be obtained via NMR detection of shear waves<sup>1</sup> or of static tissue displacement.<sup>2</sup> Here we present simulation results elucidating the effects of displacement sensitivity and applied deformation on the signal-to-noise ratio (SNR) of elasticity images obtained using static displacement, stimulated echo NMRI (SDSEI).

## PRINCIPLE

In SDSEI, the object is deformed during the stimulated echo mixing time,  $T_M$ . Local displacements are encoded by means of a pulsed gradient applied before and after deformation. The sensitivity is given by

$$\tilde{\Phi}_d = \gamma \tilde{G}_d \tau$$

where the displacement sensitivity,  $\Phi_d$ , is in radians/distance,  $G_d$  is the displacement encoding gradient strength, and  $\tau$  is the displacement encoding gradient duration. The gradient of the displacement field yields the strain field, and the strain field is used as an input for a boundary value problem to extract the tissue elastic moduli.<sup>3</sup>

## SIMULATION

A simple one-dimensional, 100-mm long object is used in all simulations. This object contains an inclusion whose shear modulus is five times larger than the surrounding material's. The pulse sequence assumed is that in the paper by Chenevert *et al.*,<sup>2</sup> with  $T_M = 200$  ms,  $\tau = 4.5$  ms, and 225 ms between displacement encoding gradients. The NMR resolution is 128 pixels. The base SNR of the material is set to 130, matching the SNR of a tissue-mimicking material measured using the SDSEI pulse sequence.

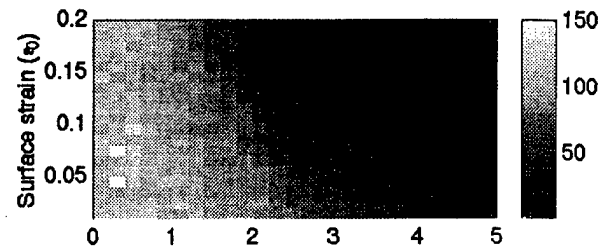
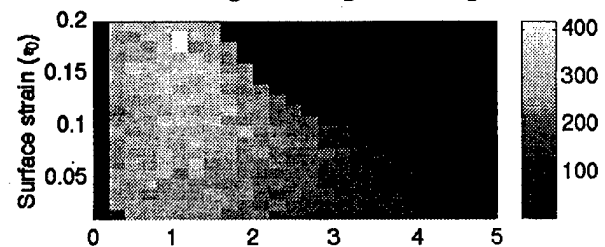
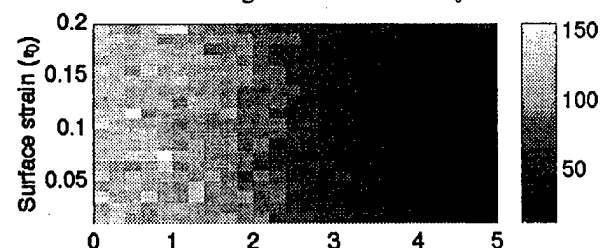
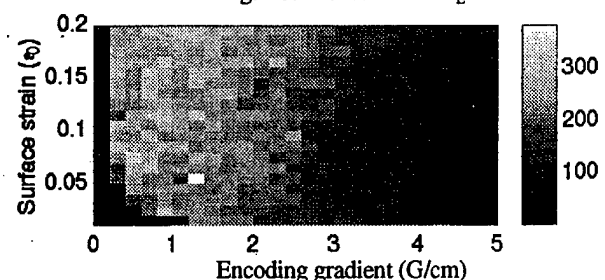
The variables used are  $G_d$  and the normalized applied surface deformation,  $\epsilon_0$ . Since  $\tau$  is assumed constant,  $\Phi_d$  varies linearly with  $G_d$ .  $G_d$  ranges from 0 to 5 G/cm in 0.2 G/cm increments, and  $\epsilon_0$  from 1% to 20% in 1% steps. For each gradient-deformation combination, both the NMR image and the elasticity image are reconstructed. The reconstructed elastic moduli are normalized to the background reconstruction. Then the NMR image SNR,  $SNR_0$ , and the elasticity image SNR,  $SNR_E$ , are calculated. Four different noise instances are averaged for every point.

## RESULTS

Figures 1a and 1b show the  $SNR_0$  and the  $SNR_E$ , respectively, of the background. Here we see that the  $SNR_0$  decreases with increasing  $G_d$  and  $\epsilon_0$  due to intrapixel dephasing. Note that signal loss due to diffusion increases as  $G_d$  increases. The  $SNR_E$  begins at 0 for  $G_d = 0$ , and then increases with both deformation and sensitivity until the intrapixel dephasing is  $\pi$  radians. Beyond this point it drops off quickly to zero. Again, diffusion signal loss is present.

Figures 2a and 2b show, respectively, the  $SNR_0$  and the  $SNR_E$  of the inclusion. Here the major source of signal loss in  $SNR_0$  is diffusion. Because the inclusion is harder than the background, it tends to displace rather than deform under the applied surface deformation; hence only the gradient contributes significantly to the intrapixel dephasing. The  $SNR_E$  simply seems to exhibit diffusion loss and does not peak as the  $SNR_E$  of the background does. Also note that the  $SNR_E$  of the inclusion is lower than that of the background.

This can be explained by noting that the elasticity reconstruction depends upon the strain field, and the strain is the gradient of the displacement field. As noted above, the hard inclusion tends to displace, not deform, under a certain surface deformation. Thus, not only does the intrapixel dephasing decrease, but the interpixel dephasing (i.e., strain) decreases. Hence the combinations of  $\Phi_d$  and  $\epsilon_0$  presented here do not approach the optimal strain fields for the inclusion reconstruction.

Fig. 1a: Background  $SNR_0$ Fig. 1b: Background  $SNR_E$ Fig. 2a: Inclusion  $SNR_0$ Fig. 2b: Inclusion  $SNR_E$ 

## CONCLUSIONS

We have illustrated the effect of displacement sensitivity and applied deformation on static displacement NMR elasticity images and noted the differing optimal imaging parameters for tissues with different shear moduli. These results suggest a type of adaptive elasticity reconstruction wherein the voxel size for a given region of tissue varies inversely with the strain field in order to optimize the elasticity reconstruction's SNR.

## REFERENCES

1. R. Muthupillai *et al.*, *Science* **269**, 1854-1857 (1995).
2. T. L. Chenevert *et al.*, *Mag. Res. Med.* **39**, 482-90 (1998).
3. A. Skovoroda *et al.*, *IEEE UFFC* **42**, 747-65 (1995).